Accepted Manuscript

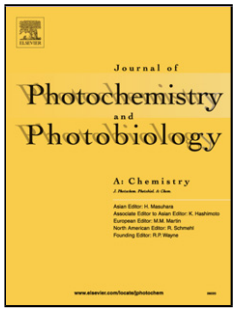

Title: Impact of the absolute rutile fraction on TiO_2 visible-light absorption and visible-light-promoted photocatalytic activity

Authors: D.M. Tobaldi, L. Lajaunie, N. Rozman, A.P.F. Caetano, M.P. Seabra, A. Sever Škapin, R. Arenal, J.A. Labrincha

PII: S1010-6030(19)30353-3
DOI: https://doi.org/10.1016/j.jphotochem.2019.111940
Article Number: 111940

Reference: JPC 111940

To appear in: *Journal of Photochemistry and Photobiology A: Chemistry*

Received date: 26 February 2019
Revised date: 14 June 2019
Accepted date: 15 June 2019

Please cite this article as: { https://doi.org/

Impact of the absolute rutile fraction on TiO_2 visible-light absorption and visible-light-promoted photocatalytic activity

DM Tobaldi,[a*] L Lajaunie,[b‡¶] N Rozman,[c] APF Caetano,[a] MP Seabra,[a] A Sever Škapin,[c] R Arenal,[bd] JA Labrincha[a]

[a] *Department of Materials and Ceramics Engineering/CICECO–Aveiro Institute of Materials, University of Aveiro, Campus Universitário de Santiago, 3810-193 Aveiro, Portugal*

[b] *Laboratorio de Microscopías Avanzadas, Instituto de Nanociencia de Aragon, Universidad de Zaragoza, 50018 Zaragoza, Spain*

[c] *Slovenian National Building and Civil Engineering Institute, Dimičeva 12, 1000 Ljubljana, Slovenia*

[d] *ARAID Foundation, 50018 Zaragoza, Spain*

*Corresponding author. Tel.: +351 234 370 041

E-mail addresses: david.tobaldi@ua.pt; david@davidtobaldi.org (DM Tobaldi)

‡Author Present Address:

Departamento de Ciencia de los Materiales e Ingeniería Metalúrgica y Química Inorgánica, Facultad de Ciencias, Universidad de Cádiz, Campus Río San Pedro S/N, Puerto Real 11510, Cádiz, Spain.

¶Author Present Address:

Instituto Universitario de Investigación de Microscopía Electrónica y Materiales (IMEYMAT), Facultad de Ciencias, Universidad de Cádiz, Campus Río San Pedro S/N, Puerto Real 11510, Cádiz, Spain.

Graphical abstract

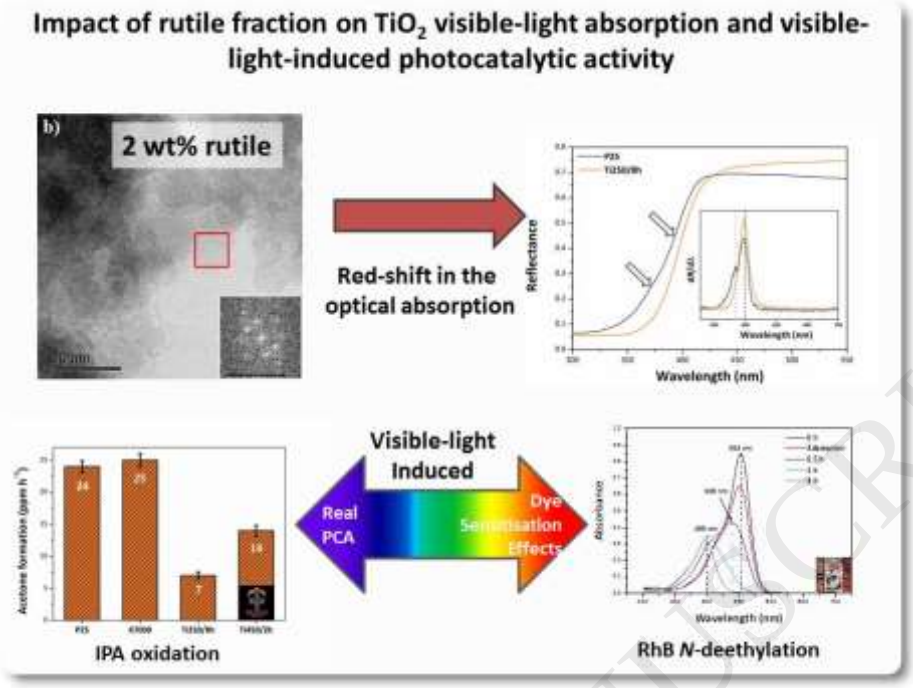

Highlights

- Phase fractions & microstructure solved *via* XRD & HR-EELS, uncommon in catalysis
- A 2 wt% rutile fraction is able to red-shift the optical E_g of the mixture
- PC activity tested in gas- and liquid-solid phase using purely visible-light
- A rutile fraction ≥10 wt% granted vis-light absorption & less charge recombination
- A rutile fraction ≥10 wt% gave real vis-light PC activity

Abstract

Titanium dioxide is by far the most used semiconductor material for photocatalytic applications. Still, it is transparent to visible-light. Recently, it has been proved that a type-II band alignment for the rutile–anatase mixture would improve visible-light absorption. In this research paper we thoroughly characterised the real crystalline and amorphous phases of synthesised titanias – thermally treated at different temperatures to get distinct ratios of anatase-rutile-amorphous fraction – as well as that of three commercially available photocatalytic nano-TiO_2.

Optical spectroscopy showed that even a small fraction of rutile (2 wt%) is able to shift to lower energies the apparent optical band gap of an anatase-rutile mixed phase. But is this enough to attain a real photocatalytic activity promoted by merely visible-light? We tried to give an answer to that question.

Photocatalytic activity was assessed in the liquid- and gas-solid phase (employing rhodamine B and 4-chlorophenol, and isopropanol, respectively, as the organic substances to degrade) using a light source irradiating exclusively in the visible-range.

Photocatalytic activity results in the liquid-solid phase showed that a high surface hydroxylation led to specimen with superior visible light-promoted catalytic activity – *i.e.* dye and ligand-to-metal charge transfer complexes sensitisation effects, not photocatalysis *sensu-strictu*.

On the other hand, the gas-solid phase results showed that a higher amount of the absolute rutile fraction (around 10 wt%), together with less recombination of the charge carriers, were more effective for both visible-light absorption and a "real" visible-light promoted photocatalytic oxidation of isopropanol.

KEYWORDS: advanced X-ray methods; high-resolution electron energy-loss spectroscopy; anatase-rutile mixture; apparent optical band gap; visible-light

1. Introduction

1972 was the year when Honda and Fujishima firstly demonstrated electrochemical photolysis of water using a titanium dioxide (TiO_2, titania) electrode (and a Pt counter-electrode) [1]. Since then, the research about TiO_2 and its photocatalytic (PC) application has been growing exponentially [2]. Indeed, TiO_2 still remains the most widely used oxide for PC applications, owing to its low cost, high activity, and stability in both basic and acidic media [3].

TiO_2 crystallises in a large number of polymorphs [4], though anatase and rutile are the most widely used for PC applications, with anatase believed to have better PC performances than rutile [5,6]. [This is the reason why the vast majority of the research to improve the PC performances and extend its light absorption to the visible (see below), is headed to the anatase TiO_2 polymorph.] TiO_2 electronic configuration retains zero 3*d* electrons, and the optical band gap (E_g) of anatase and rutile is accepted to be around 3.2 and 3.0 eV [7], respectively, thus being transparent for most of the visible radiation region. This means that the PC reaction is exploited by 3–5% of the solar spectrum [8], this is the reason why the scientific community is challenging in extending its light response to the visible-region [9].

First attempts to modify TiO_2 electronic structure were made by doping TiO_2 with transition metals [10]. However, this strategy proved itself to be counterproductive, because transition metals behaved as recombination centres for the photo-generated couple e^-/h^+ [11]. Then, researcher successfully synthesised TiO_2 with Ti^{3+} dopants. This so-called "Ti^{3+} self-doping" is a technique to harvest visible-light without introducing any foreign element into titania structure [12]. However, to be successful, this method involves toxic precursors and solvents, *i.e.* hydrofluoric acid (HF), TiF_4 and $TiCl_3$ [12,13], thus being contrary to most of the principles of green chemistry – photocatalysis can be certainly considered as one of the most innovative approaches in green chemistry [14].

Asahi and co-workers succeeded in doping TiO_2 with nitrogen, thus extending titania's light response to the visible [15]. However, also this approach proved itself to be somehow unsuccessful. Indeed, if from one hand anionic doping extends TiO_2 light absorption to the visible, from the other it is reasonable that, during the oxidising working conditions of a PC reaction, titania might have a "self-cleaning" disposition, ejecting N^{3-} anions from the structure [16] – provided that nitrogen is present in the nitride state. The photocatalyst is thus not stable and cannot be recycled after repeated PC runs [17].

Other strategies adopted to extend TiO_2 light response to the visible region were to graft / decorate its surface with noble-metals atoms [18–21] – although effective, these methods proved to be quite expensive. It was even found that high-pressure cubic TiO_2 would absorb visible-light, but those phases are not stable at atmospheric pressure, thus unsuitable for real-world PC applications [22,23].

The investigations reported so far mainly regarded the doping and/or modifications of the anatase TiO_2 polymorph. However, Degussa P25 is known to be one of the most effective commercial TiO_2-based photocatalysts. This is a mixture of nano-anatase and nano-rutile, as well as some amount of amorphous fraction [24], and it possesses some weak absorption into the visible region [25]. From this starting point, very recent literature has been paid to investigate the electronic structure of anatase/rutile mixed-phase TiO_2 nano-powders [26], and its possible synergy in PC reactions [27]. As a matter of fact, it is believed that the phase junction of nanocomposite materials is key to obtain improved PC performances [28]. Scanlon *et al.* showed that a type-II (staggered) band alignment of ~0.4 eV exists between anatase and rutile TiO_2 polymorphs when they form a hetero-junction, with anatase possessing the higher electron affinity [29]. This was further confirmed by a very recent work of Nosaka and Nosaka, who suggested that, in an anatase-rutile hetero-junction, the conduction band bottom (E_{CB}), for the indirect E_g of 3.2 eV, should be 0.4 V lower than the E_{CB} of rutile TiO_2.[30] Indeed, such band alignment has a twofold advantage [31]: (i) on excitation, it is beneficial for electrons to flow from rutile to anatase, and for holes to flow in the opposite direction, this leading to efficient separation of the charge carriers. (ii) The effective E_g of the mixture is lower than that of the constituent polymorphs, this leading to enhanced visible light absorption.

Aware of these findings, the quest for attaining a visible-light activated PC material showing good performances might be closed by investigating anatase-rutile hetero-junctions composed of different fraction of anatase and rutile (and amorphous phase) [32]. Therefore, in this work, the real crystalline/amorphous composition of several synthesised and commercial TiO_2-based PC nanoparticles (NPs) was thoroughly explored *via* X-ray powder diffraction (XRPD), and the materials fully characterised. This is a very innovative approach within the catalysis community, as TiO_2 absolute crystallinity has been rarely determined [33–38]. Furthermore, it has been shown that the amorphous fraction of TiO_2 has no or little PC activity [39], this also influences the interpretation of the results.

The PC activity was evaluated using exclusively visible-light irradiation from a white LED lamp source, in the liquid-solid as well as gas-solid phase. In the former, the PC activity was assessed monitoring the decolouration of an organic dye, rhodamine B (RhB) and the degradation of a phenolic compound (highly toxic and poorly biodegradable compounds) [40], 4-chlorophenol (4-CP). In the latter, isopropanol was used as the organic substance to degrade.

2. Experimental section

2.1 Sample preparation

An adapted aqueous sol-gel method, developed by the authors, was used for the synthesis of TiO_2-based photocatalysts; very detail of it can be found elsewhere [41]. Briefly, sols were synthesised *via* the controlled hydrolysis and peptisation of titanium(IV)isopropoxide (Ti-*i*-pr, $Ti(OCH(CH_3)_2)_4$) with Milli-Q water (18.2 MΩ cm, H_2O:Ti-*i*-pr = 4:1) diluted in isopropyl alcohol (IPA). To get different anatase-to-rutile-to-amorphous ratios, dried gels were thermally treated at different temperatures, with different dwell times, always under a static air flow, and using an electric muffle furnace. In detail: samples were thermally treated up to: (i) 250 °C with a heating rate of 15 °C min^{-1}, pre-heating the furnace at 200 °C, with a 8 h dwell time (**Ti250/8h**); (ii) 450 °C, and (iii) 800 °C with a heating rate of 5 °C min^{-1}, with a 2 h dwell time (samples were designated as **Ti450/2h** and **Ti800/2h**, respectively).

Commercial TiO_2-based, nanostructured photocatalysts – chosen because they are among the most widely employed in photocatalysis – were also used, with a view to compare their phase composition and PC activity with that of our synthesised titanias. These were: AEROXIDE® TiO_2 P25 (formerly known as Degussa P25, here designated as **P25**), that is a mixture of nano-anatase, nano-rutile and amorphous phase [24], Hombikat UV 100 (**HK-UV100**), an unmodified nano-anatase, and KRONOClean 7000® (**K7000**) – a carbon-modified nano-anatase, known to be a visible-light active photocatalyst [42]. Commercial photocatalysts were all used as received.

2.2 Sample characterisation

XRPD was used to get information about the real crystalline and amorphous fraction in the specimens. For this purpose, XRPD patterns for full quantitative phase analysis (FQPA) were recorded at room temperature (RT) on a θ/θ diffractometer (PANalytical X'Pert Pro, NL), equipped with a fast RTMS detector (PIXcel 1D, PANalytical), with Cu Kα radiation (45 kV and 40 mA, 20–80 °2θ range, with a virtual step scan of 0.0263 °2θ, and virtual time per step of 200 s). Divergence and antiscattering slits of 0.5°, as well as a Soller slit of 0.04 rad were mounted in the incident beam pathway. A Ni filter and a 5 mm anti-scatter blade were in the diffracted beam pathway; the specimens were loaded on a zero-background monocrystalline Si sample-holder. FQPA was assessed using the combined Rietveld and reference intensity ratio (RIR) methods, as previously reported by Gualtieri and co-workers [43,44]. More specifically: 10 wt% α-alumina (NIST SRM 676a) with certified phase purity being 99.02±1.11 wt% [45], was added to the sample, and treated as an additional phase in the refinements. In this way, the refined weight fractions of each crystalline phase (W_{ic}) were rescaled with respect to the known weight fraction of the added standard (W_s), with the purpose of obtaining the real crystalline phase weight fraction (W_i), according to:

$$W_i = \frac{1}{1-W_s}\left[\left(\frac{W_S}{W_{SC}}\right) W_{ic}\right] \quad (1)$$

In (1), W_{sc} is the refined weight fraction of the internal standard. Therefore, knowing the weight fractions of all the crystalline phases, the amorphous content (W_a) is given by the difference between 1 and the "as-received" components (W_i), *i.e.* the TiO_2 polymorphs in the specimens:

$$W_a = 1 - \sum_i W_i \quad (2)$$

The errors associated with the calculation of both the amorphous and crystalline phase fractions were calculated according to the procedure proposed by Madsen and Scarlett.[46]

The Rietveld data analysis was assessed using the GSAS software package [47], and its graphical interface EXPGUI [48]. Instrumental broadening, obtained from the refinement of LaB_6 standard (NIST SRM 660b), was taken into account in all of the Rietveld refinements. These latter were accomplished by refining the following parameters: scale-factors, zero-point, 6 coefficients of the shifted Chebyshev function to fit the background, unit cell parameters. The profile was modelled using the Thompson-Cox-Hasting formulation of the pseudo-Voigt function [49], and two Lorentzian (L_X and L_Y) terms, peak correction for asymmetry, as well as sample displacement effects, were refined. The Gaussian parameter (G_W, an angle independent term) of the pseudo-Voigt profile shape function of the phases constituting the samples was instead constrained to the value obtained for α-alumina (NIST SRM 676a). The starting atomic parameters for anatase, rutile, and brookite when present, described in the space groups (SGs) $I4_1/amd$, $P4_2/mnm$ and

Pbca respectively, were taken from the literature [50–52]. Furthermore, aiming at estimating FQPA precision, both the sample preparation and data collection were repeated in triplicate per each specimen (three different batches, in the case of commercial photocatalysts), and the confidence interval (CI) at 95%, reflecting a significance level of 0.05, was then calculated using *t*-statistic.

Microstructural features of the specimens were also determined *via* XRPD, using the same instrument and setup as per the FQPA, but in the 20−145 °2θ range, with a virtual step-scan of 0.1 °2θ, and virtual time per step of 500 s, so to have data with a higher signal-to-noise ratio. The whole powder pattern modelling (WPPM) [53,54], as implemented in the PM2K software [55], was used for the microstructural analysis of the diffraction data. WPPM is a novel yet state-of-the art technique; it exploits XRPD by describing each observed peak profile as a convolution of instrumental and sample-related physical effects, and refining the corresponding model parameters directly on the observed data [56,57]. This way, adopting the WPPM formalism, microstructure information (*i.e.* crystalline domain shape, size distribution, defect type, and content) can be obtained quantitatively [58,59]. Indeed, it is quite rare in the catalysis community to extract robust and physically meaningful microstructural information: as a matter of fact, this kind of information is usually extracted using integral breadth methods for line profile analysis (LPA) – *inter alia* the Scherrer formula [60], the Williamson−Hall plot [61], or the Warren-Averbach analysis [62]. On the contrary, results given by the WPPM outshine – in terms of both quality and quantity – those frequently obtained in the catalysis community using said LPA methods. This is because traditional LPA techniques are essentially based on simplified hypotheses (often not met), and thus the corresponding results are hard to interpret in terms of physical quantities that could be measured alternatively with other techniques, like microscopy. Thus, with the WPPM formalism, all of the effects contributing to the line profile are considered, and physical parameters are directly determined from the experimental data without any intermediate stage of profile fitting [63]. In this work, considering the nanocrystalline nature of the domains, these were assumed to be strain free and their shape was approximated to be spherical with diameter distributed according to a log-normal curve (*i.e.* strain contributions to the peak profile were neglected, and peak broadening was assumed isotropic). The instrumental contribution was obtained by parametrising the profile of 18 *hkl* reflections from the NIST SRM 660b standard (LaB_6), according to the Caglioti *et al*. relationship [64]. To assess the WPPM modelling we used the anatase (SG $I4_1/amd$), rutile (SG $P4_2/mnm$) and, when present, brookite (SG *Pbca*) phases; then these parameters were refined: background (that was modelled using a 6th-order Chebyshev polynomial), peak intensities, specimen displacement, lattice parameters, mean and variance of the log-normal size distributions.

Aberration corrected high-resolution scanning transmission electron microscopy (HR-STEM) experiments have been performed using a FEI Titan Low-Base microscope operated at 300 kV and equipped with a CESCOR Cs probe corrector, an ultra-bright X-FEG electron source, a monochromator and an energy-

dispersive X-ray spectroscopy (EDS) detector. HR-STEM imaging was performed by using high-angle annular dark field (HAADF) and annular bright field (ABF) detectors. Automatic interpretations of the fast Fourier transform (FFT) patterns were performed by using the JEMS software [65]. Spatially-resolved electron energy loss spectroscopy (SR-EELS) experiments were performed with a monochromated beam. To check the homogeneity of the samples, several areas per sample were probed, however only the most representative spectra are shown here. The energy resolution was 210 meV with a dispersion of 0.03 eV per pixel and the acquisition time was about 0.18 second per pixel (total acquisition time ~70 seconds) for core-loss spectra. The acceptance and convergence angles were 10 and 34 mrad, respectively. The datasets were de-noised by using the principal component analysis routines of the HyperSpy software package [66].

Diffuse reflectance spectroscopy (DRS) was used to obtain information about the apparent optical E_g of the specimens, as this is a key-point for PC applications. Optical spectra were acquired on a Shimadzu UV-3100 spectrometer (JP), equipped with an integrating sphere and a white reference material made of Spectralon®; spectra of the samples were recorded in the UV–Vis range (250–750 nm), with 0.2 nm step size. As the apparent optical E_g is a key-issue for PC applications, this was calculated through the Tauc formalism [67], and also the differential reflectance method [68]. According to the former, the band-to-band transition in a semiconductor material is defined by:

$$\alpha h\nu = A(h\nu - E_g)^{\gamma} \quad (3)$$

In equation (3), *h* is the Planck's constant; *v* is the frequency of the light; *A* is a material constant; E_g is the optical energy band gap of the allowed transitions; the power coefficient *γ* is characteristic for the type of transition – it is considered to be equal to 1/2 or 2 depending on whether the type of transition is directly allowed, or indirectly allowed, respectively [67]. The first term of the Tauc formula, *α*, is the pseudo-absorption coefficient, which is derived from the Kubelka-Munk theory [69]:

$$\alpha \approx \frac{K}{S} = \frac{(1-R_\infty)^2}{2R_\infty} \equiv F(R_\infty) \quad (4)$$

In which *K* and *S* are the absorption and scattering coefficients (*S* of most materials are relatively invariant along the visible range of the optical spectrum, so it can be treated as a constant), respectively; *R* is the reflectance. Thus, applying the Tauc plot, the apparent optical E_g of a semiconductor material can be achieved from the *x*-axis intercept (*i.e.* $\alpha = 0$) of the line which is tangent to the inflection point of the $(\alpha h\nu)^{1/\gamma}$ *versus* $h\nu$ curve. In this work, this was found by fitting the transformed Kubelka–Munk equation against the photon energy ($h\nu$) with a sigmoidal Boltzmann function (*via* the Origin ProLab software package, version 8.5.0). In the latter method, it is presumed that the apparent optical E_g of a semiconductor material is given by the maximum value of the plot originated by the first derivative of reflectance *versus* the wavelength ($dR/d\lambda$).

Raman spectroscopy was used to investigate the disorder into the TiO_2 structures. Raman spectra were recorded using a RFS 100/S (Bruker, DE) equipped with a 1064 nm Nd:YAG laser as the excitation source, in the 50–1000 cm^{-1} wavenumber range, with 2 cm^{-1} resolution.

FT-IR spectra, in attenuated total reflectance (ATR) mode, were recorded on a Bruker Tensor 27 (DE) spectrometer, in the wavenumber range of 4000–350 cm^{-1}. This was done to detect the occurrence of OH groups and/or water adsorbed on the photocatalyst surface.

Photoluminescence (PL) spectra were recorded at RT, in the visible spectral range, with a modular double grating excitation spectrofluorimeter with a TRIAX 320 emission monochromator (Fluorolog-3, Horiba Scientific, JP) coupled to a R928 Hamamatsu photomultiplier, using a front face acquisition mode. The excitation source was a 450 W Xe arc lamp. The emission spectra were corrected for detection and optical spectral response of the spectrofluorimeter, and the excitation spectra were corrected for the spectral distribution of the lamp intensity using a photodiode reference detector.

The specific surface area (SSA) of the specimens was measured using the Brunauer–Emmett–Teller (BET) method (Micromeritics Gemini 2380, US) by means of N_2 as the adsorbate gas, on samples degassed at 120 °C.

Dynamic light scattering (DLS) measurements were recorded at RT using a Zetasizer Nano ZS (Malvern Instruments, UK). The scattering was measured at an angle of 173°, using a 633 nm laser, and the refractive indexes of water and the TiO_2 NPs were assumed to be 1.33 and 2.50, respectively. Reported results are averaged over three consecutive measurements (each measurement consisting of 15 runs).

2.3 Photocatalytic activity

2.3.1 Liquid-solid phase

A detailed description of the PC tests assessed in the liquid-solid phase is reported in the *Supplementary Information Material*.

2.3.2 Gas-solid phase

The device employed for the gas-solid phase PC activity tests is a cylindrical reactor (1.4 L in volume) covered by a quartz glass connected by Teflon tubes to a FT-IR spectrometer; the whole system was hermetically sealed. IPA was chosen as the pollutant to degrade, and the principle behind that technique is presented in very detail elsewhere [70–72].

IPA was chosen because its photocatalytic oxidation is as follows: IPA $\xrightarrow{k_1}$ acetone $\xrightarrow{k_2}$ further products → CO_2 + H_2O. According to Munuera and colleagues [73,74], the IPA to acetone reaction is a zero order reaction, whilst the second reaction (acetone to further products) is a first order reaction. Furthermore, Larson *et al*. [75], demonstrated that k_1 >> k_2, therefore, we can safely assume the initial reaction rate of acetone formation to be reasonably approximated as linear, and obtain a reliable kinetic for the PC activity.

The light source employed for the PC tests was a 300 W Xenon lamp (Newport Oriel Instruments, US). The lamp imitates solar light spectrum, both in the UV and visible range. To exclude the UV light, a 400 nm cut-off filter was used, and thus measurements were taken only under visible-light irradiation. The filter decreases the light intensity, which reaches a value of 8.5 mW cm^{-2} in the 400–800 nm range. Samples used in these tests were prepared in the form of a thin layer of powder with a constant mass (about 50 mg), and therefore approximately constant thickness, in a petri-dish having 6 cm in diameter. The working distance between the petri-dish and the lamp was 6 cm. The relative humidity in the reacting system was kept constant in the range 25%–30% by means of a flow of air passing through molecular sieves until a pre-defined humidity was attained. Each experiment was performed by injecting 8 µL of IPA (~800 ppm in gas phase) into the reacting system through a septum; the total reaction time was set at 24 h, and the lamp was turned on after a certain period of time after IPA injection, to allow for an equilibration of IPA adsorption onto the powder. IPA degradation, as well as the acetone formation-degradation process, was followed by monitoring the calculated area of their characteristic peaks at 1104 and 1207 cm^{-1}, respectively, by using a FT-IR spectrometer (Perkin Elmer Spectrum BX, US). The acetone formation kinetics was taken as a measurement of PC activity, because the only source of acetone is PC oxidation of IPA. On the other hand, the decreasing concentration of IPA may come about due to PC activity and some other unintended processes, like adsorption and possible minor leaking.

3. Results and discussion

3.1 Microstructural, chemical and FQPA analyses: HR-STEM, EELS and XRPD

Fig. 1a,b depicts the HR-STEM micrographs of sample **Ti250/8h**. This sample is made of clustered NPs with a diameter typically ranging typically between 3 and 9 nm. The crystalline nature of the NPs is clearly seen in all the micrographs and also in the FFT pattern (inset of Fig. 1b). However, automatic indexation of the FFT pattern by the JEMS software yields solution for both the anatase and brookite phases, thus it is not possible to discriminate the TiO_2 polymorphs only by quantitative image analysis. To get more information on the chemical nature of the nanoparticles, SR-EELS spectra were recorded on different areas of 50 × 50 nm (Fig. 1c). Beyond elemental quantification, EELS analyses in the core-loss region can provide meaningful

information related to the local chemical environment, such as the valence state, the local site symmetry, and bonding nature [76–79]. Fig. 1d shows a representative spectrum of the sample **Ti250/8h**, around the Ti-$L_{2,3}$ edges, which are related to Ti *2p* transitions. The L_3 (situated between 455 and 461 eV) and L_2 (situated between 461 and 467 eV) edges are split in two lines as a consequence of the crystal field splitting of the t_{2g} and e_g orbitals [80,81]. The shape of the spectrum is influenced by the local site symmetry and band-structure effects: this can be used to distinguish the three TiO_2 polymorphs [82]. In particular, the L_3 line situated at higher energy (highlighted by an arrow in Fig. 1d) is the fingerprint of the crystallographic phases.[81,82] In case of the sample **Ti250/8h**, the shape of the Ti-$L_{2,3}$ edges is a clear gauge of anatase phase [81]. It should be noted that no variation in fine structures is observed on the probed area. This means that the sample is quite homogeneous at the nanometre scale. Fig. 2a,b shows the STEM micrographs of sample **Ti450/2h**. This is also made of clustered NPs with diameters ranging between 4 and 60 nm. Most of the NPs are crystalline, as it can be clearly seen from Fig. 2b. However, the indexation of The FFT patterns is not conclusive. In particular, the FFT, inset of Fig. 2b, can be indexed as anatase in the [001] zone axis, but also as brookite in the [100] zone axis. Fig. 2d shows three representative EELS spectra for this sample. Several variations of the Ti-$L_{2,3}$ fine structures can be seen in the probed area, highlighting the chemical inhomogeneity at the nanoscale for this sample. In particular, spectrum A (red line in Fig. 2d) indicates the presence of the anatase crystallographic phase, while spectrum B (blue line in Fig. 2d) could correspond to the rutile crystallographic phase. The spectrum C (green line in Fig. 2d) indicates a mix of anatase and rutile and/or the presence of the brookite phase.

Fig. S2a,b shows HR-STEM micrographs of the sample **HK-UV100**. This sample is made of small NPs strongly clustered and with a diameter between 3 and 10 nm. The crystalline nature of the NPs is clearly seen in Fig. S2a,b, even if some areas of the sample seem to be amorphous (red arrows in Fig. S2b). Fig S2c depicts two representative EELS spectra taken on two different areas. The spectrum A is characteristic of anatase TiO_2 polymorph. The spectrum B is completely different, and is observed less frequently than the spectrum A. In particular, the L_3 and L_2 edges are not split, this being a characteristic of amorphous TiO_2 [82].

DLS measurements confirmed that the analysed NPs were prone to clustering, *via* aggregation/agglomeration, also in the liquid medium, as shown in Fig. S3a-e. Their (hydrodynamic) diameters are reported in Table S1.

XRPD patterns of prepared samples, as well as of commercial specimens, are reported in Fig. 3a,b. A graphical output of a Rietveld FQPA refinement is displayed in Fig. S4; whilst FQPA results employing the Rietveld-RIR method are listed in Table 1. In the synthesised specimens, the fraction of anatase, rutile, brookite and amorphous phase varies with the thermal treatment. As it is seen in Table 1, specimen **Ti250/8h** is mainly composed of anatase (88.5 wt%, with a CI at 95% of ±1.9), rutile (2.0 wt%; CI = ±0.7), amorphous phase (6.0 wt%; CI = ±3.9), and a small amount of brookite fraction (3.4 wt%; CI = ±1.6). An

increase in the thermal treatment, specimen **Ti450/2h**, is reflected by a rise in the anatase-to-rutile phase transition (ART). This specimen is made of a less anatase fraction, 70.2 wt% (CI = ±1.8), but a higher amount of rutile and brookite, 15.4 and 6.7 wt%, respectively, and also amorphous phase, 7.6 wt% (CI = ±2.6). The presence of brookite is due to the acidic conditions of the synthesis method.[83,84] Furthermore, a longer dwell time at 250 °C (*i.e.* 8 h), favoured to some extent the crystallisation of anatase at the expense of the amorphous phase – as a matter of fact, **Ti250/8h** has 6.0 wt% amorphous, whilst **Ti450/2h** 7.6 wt%. At 800 °C, ART is accomplished: specimen **Ti800/2h** is virtually composed of crystalline rutile only.

As per the commercial specimens, anatase is the unique crystalline phase in both **K7000** and **HK-UV100**. **K7000**, as we reported previously, contains 92.8 wt% anatase (CI = ±1.5), and 7.2 wt% amorphous phase (CI = ±1.5) [42]. **HK-UV100** contains a higher amount of amorphous phase, 20.9 wt% with a CI of ±1.5, this being in contrast with findings reported in previously published literature, which found an even higher amount of amorphous phase in **HK-UV100**, *i.e.* around 30% [33,36]. On the other hand, **P25** is composed of anatase (78.6 wt%; CI = ±5.7), rutile (10.7 wt%; CI = ±2.6), and amorphous phase (10.6 wt%; CI = ±4.2).[24] The anatase-to-rutile wt% ratio, in the crystalline fraction of **P25**, is 88:12, in line with what reported previously [24,36,85]. However, given the large values of CI, it is conceivable that the phase composition of **P25** greatly fluctuates amongst the three different batches used for the FQPA, this being fully consistent with the findings reported by Ohtani *et al.* [85], and with the data published by Lebedev *et al*. [36]. On the other hand, the values found in this work are in contrast with those of Jensen and co-workers [33], who stated **P25** to be close on being fully crystalline, consisting of 73% anatase, 18% rutile and 9% amorphous – they also claimed the amount of amorphous material to be overestimated.

Microstructural features of the synthesised titanias are shown in Fig. 4a-c, and Table 2; an example of a WPPM graphical output is illustrated in Fig. S5. The average diameter of anatase crystalline domains in **Ti250/8h** is 4.4±0.1 nm, that of rutile 8.7±1.4 nm. As displayed in Fig. 4a, both the size distributions have positive skewness [*i.e.* 0.8(1) and 0.9(1), respectively], with a low polydispersity index (PDI), equal to 0.06(1) and 0.09(3) for anatase and rutile, respectively (Table 2), depicting narrow size distributions. Furthermore, anatase NPs are described by a narrower size distribution than that of rutile (the mode being 4.1±0.1 nm, and 7.6±1.2, respectively). As per **Ti450/2h**, the increase in thermal treatment also led to an increase in the average size of anatase and rutile crystalline domains – ART being a nucleation-and-growth phenomenon [86]. Anatase grew to an average size of 11.0±0.1 nm, whilst rutile almost doubled its diameter compared to that at 250 °C, this being: 16.1±0.1 nm – both anatase and rutile are described by moderate size distributions, the PDI being 0.11(1) and 0.23(4), respectively, as well as positive skewness. At 800 °C, **Ti800/2h**, ART is complete and, following the nucleation-and-growth mechanism, the rutile mean crystalline domain diameter increased, attaining 89.4 nm [PDI = 0.13(3)].

Following on from our earlier studies, we have already shown that the average crystalline domain diameter of anatase and rutile in commercial **P25** is 15.5±0.3 and 19.3±0.6 nm, respectively [24]. PDI of anatase size distribution is 0.18(1), with positive skewness [1.4(1)], and mode being 12.1(3) nm. Rutile, on the other hand, has a higher PDI, this being 0.29(6), positive skewness [1.8(1)], but it is described by a broader size distribution, the mode being 13.0(4) – as also suggested by its larger PDI value. **K7000** and **HK-UV100**, despite being anatase the only crystalline phase, have a more complex microstructure. Tobaldi *et al*. [42], taking advantage of XRPD and WPPM, reported **K7000** to be described by a bimodal size distribution of anatase crystalline domains, mostly 4 nm in diameter, but with a small amount of a larger fraction between 12 and 15 nm – the diffraction results were confirmed by HR-TEM investigations. Similarly, **HK-UV100** shows complex microstructural features, *cf* Fig. 5. The fitting using a unimodal size distribution did not give satisfactory results: this is highlighted by the difference curve, the continuous black line in Fig. 5, meaning that some features are still present, probably because of a non-ideal distribution of crystalline domains. Assuming a bimodal model for the probability distribution, we obtain a better fit, as shown in Fig. 5 by the difference curve marked with a continuous blue line. Adopting the bimodal model, anatase crystalline domains of 2.0±0.1 nm in diameter co-exist together with a smaller population of a larger-sized fraction of anatase (having an average diameter of 9.9±0.4 nm). Both log-normal size distributions have a right-hand tail (*i.e.* positive skewness), and the larger-sized fraction of anatase has a lower PDI than that of the smaller-sized – 0.09(1) *versus* 0.28(8). These results contrast those of Lindner *et al*. [87], and those of Chen and Ray [88], who reported **HK-UV100** to be composed of anatase nanocrystals having size of 5 nm, and approximately 6 nm, respectively. On the contrary, they are partly consistent with those of Jensen *et al.* [33], who stated that **HK-UV100** has a complex structure, and also assumed it to be composed of "two sizes" – through small–angle X–ray scattering (SAXS) measurement – but they assigned the smaller fraction to the amorphous phase present in **HK-UV100**, and the larger fraction to crystalline anatase – 3.9 and 50.9 nm, respectively, in reference [33]. Results regarding the crystalline domain diameters confirm the HR-STEM observations.

3.2 Spectroscopic analyses

The results of Kubelka-Munk analyses of the optical data are shown in Fig. 6. In these, a single absorption band is noticeable for all the spectra in the high energy region (*i.e.* < 360 nm), that is typically associated with the band-to-band transition in titania [89]. The onset of the absorption edge is different amongst the entire set of specimens, shifting to lower energies in the synthesised specimens. That behaviour reveals dissimilar apparent optical E_g values. For this reason, and being the optical E_g a key-factor for PCA application, this was determined using both the Tauc procedure and the differential reflectance method; results are listed in Table 3. An indirect nature is widely attributed to the interband transition in anatase,

whilst rutile is accepted to belong to the family of direct E_g semiconductor materials [90,91]. On the other hand, there is still no utter consensus among the scientific community about the transition in the E_g of brookite; nevertheless, this is located well in the UV region, being reported to be around 3.4–3.3 eV (~365–376 nm) [92,93]. Therefore, when using the Tauc procedure, we examined plots of $(\alpha h\nu)^{\gamma}$ *versus* photon energy, with γ = ½ or 2, to define the apparent optical E_g. As shown in Table 3, an indirect transition to anatase, and a direct one to rutile (*i.e.* specimen **Ti800/2h**), agree well with previous literature data [5,91]. Actually, looking at the synthesised specimens, Table 3, apparent indirect optical E_g values of **Ti250/8h**, and **Ti450/2h** are 3.05 and 2.99 eV, respectively, thus shifted toward the visible-range. Similarly, a direct band-to-band transition for **Ti800/2h**, giving an E_g value equal to 3.07 eV, is consistent with the expected rutile direct E_g value of 3.0 eV [5,91]. Thus, the observed red-shifting in **Ti250/8h**, **Ti450/2h** is indeed due to the presence of rutile. Furthermore and most importantly, even a small amount of rutile (*i.e.* 2.0 wt% in **Ti250/8h**) is effective in shifting titania apparent optical E_g toward the edge of the visible region. Therefore, endorsing what theoretically calculated by previous literature [29].

As per the commercial specimens, the apparent indirect optical E_g of **K7000** and **HK-UV100**, being equal to 3.28 eV for both the samples, is perfectly consistent with their phase composition, thus with the expected E_g of anatase [5,91]. **P25** deserves special attention: its apparent indirect optical E_g is at 3.06 eV, thus it is also red-shifted compared to that expected for anatase TiO_2 (*i.e.* around 3.2 eV) [5,91]. On the contrary, adopting the direct E_g model for **P25**, we achieved a larger optical E_g, 3.50 eV (354 nm), therefore being in contrast with most of the available literature data.

However, looking at the DRS spectra of **Ti250/8h** and **P25**, *cf* Fig. 7, the slope of the absorption feature in the 300–400 nm region – that typically associated with absorption across the bandgap in TiO_2 NPs – has different trends. In case of **Ti250/8h**, that slope is steady; on the contrary, that of **P25** is characterised by the presence of two steps, as highlighted by the arrows in Fig. 7. This is indeed caused by two distinct band-to-band transitions, as better revealed in the inset of Fig. 7, where is reported the first derivative of reflectance against the wavelength λ. In it, one transition is assigned to anatase (E_g at 3.34 eV, dash-dotted line in the inset of Fig.7), the other to rutile (E_g at 3.11 eV, dashed line, inset of Fig. 7) [94]. This implying **P25** to be mainly composed by individual anatase and rutile NPs, in some way confirming a very recent work by Jiang *et al* [95]. By contrast, the plot of the first derivative of reflectance *versus* λ in **Ti250/8h** displays only one local maximum, suggesting that – being here anatase and rutile NPs in a more intimate contact, forming a hetero-junction, as shown in Fig. 1a,b – a small amount of rutile (*i.e.* 2.0 wt%) is able to give a single band-to-band transition (at around 3.10 eV, 400 nm). This is consistent with recent results obtained by Celik *et al*. [94], who demonstrated rutile possessing a stronger relative response factor for diffuse reflectance than that of anatase. [For sake of clarity, this also happens for **Ti450/2h**, whose dR/dλ plot is not reported here; refer instead to Table 3.] Therefore, for this system, the differential reflectance

method (*cf* Table 3, sixth to ninth columns), seems to be the most suitable for estimating the apparent optical E_g [96].

Raman spectra are shown in Fig. S6, whilst the position and full width at half maximum (FWHM) of Raman E_g mode of anatase are listed in Table 4. A shift toward higher energies of that Raman mode, as well as a broadening in its FWHM have been reported to be due to phonon confinement, non-stoichiometry, internal stresses and changes in the size of anatase nanocrystals [97]. For instance, Zhang and co-workers found that Raman E_g mode to be at 143.5 cm^{-1}, with a FWHM of 9 cm^{-1} on anatase NPs having 27.9 nm in size [98]. Li Bassi *et al*., studying anatase NPs with 33 nm in diameter, found them having a FWHM value of ~13 cm^{-1}, and a position of ~145.6 cm^{-1} [99]. The values of E_g Raman band position and FWHM listed in Table 4 are blue-shifted, and their FWHM are broader compared to these literature data [98,99], this confirming the very reduced dimensions of the anatase crystalline domains found with both diffraction and microscopy (*cf* Table 2, and Figs. 1 and 2).

FT-IR spectra, reported to show the existence of surface adsorbed water, are depicted in Fig. S7a,b. The strong asymmetric band with its maximum at around 3100 cm^{-1} depicts the presence of adsorbed molecular H_2O, which also gives rise to the feature near 1630 cm^{-1}, that is due to H–O–H bending [100]. Among the synthesised specimens, **Ti250/8h** is that adsorbing more water from the atmosphere; **HK-UV100**, that with the strongest feature at ~3100 cm^{-1} between the commercial set of samples.

3.3 Visible-light photocatalytic activity

3.3.1 Liquid-solid phase

Liquid-solid phase PC tests with the visible-light LED lamp showed that RhB was essentially decoloured *via* dye sensititsation effects, as shown in Scheme 1a. The same happened to 4-CP: its disappearance under visible-light irradiation was due to the formation of ligand-to-metal charge transfer complexes (LMCTC) on TiO_2 surface, which is known to induce visible light absorption. As photo-oxidation by direct excitation of TiO_2 did not (likely) happen, a detailed description of liquid-solid phase PC tests is reported in the *Supplementary Information Material*. The main text will be focussed on the gas-solid phase results.

3.3.2 Gas-solid phase

PC activity results of the samples in the gas-solid phase regime – shown as the formation rate of acetone (ppm h^{-1}), which is a measure of the PC activity – are summarised in Fig. 8. Although liquid-solid and gas-solid phase PC activities cannot be directly compared, the difference amongst the reaction rates obtained in the liquid-solid phase is evident (*cf Supplementary Information Material*). **P25** and **K7000** are the most

active specimens, having an acetone formation rate of 24 and 25 ppm h^{-1}, respectively. Both the synthesised samples, **Ti250/8h** and **Ti450/2h**, show a lower PC activity: 7 and 14 ppm h^{-1}, respectively. However, conversion of IPA to generate acetone under direct visible-light irradiation clearly suggests that photo-oxidation of TiO_2 by direct excitation took place.

3.3.3 Mechanistic aspects of photocatalytic activity

Key-factors of PC activity are: optical E_g, SSA and particle size (intimately related to each other), and availability of OH surface groups [101]. According to the FT-IR analysis, **Ti250/8h** was the specimen with stronger bands due to adsorbed H_2O and H–O–H surface groups, this being in favour of its PC activity, refer to Fig. S7a. **Ti250/8h** has also the highest SSA (134.4 m^2 g^{-1}), whilst those of **Ti450/2h** and **P25** are comparable (45.9, and 52.5 m^2 g^{-1}, respectively), this indeed being of further benefit for **Ti250/2h**, see Table 3. Consistent with the higher SSA, **Ti250/8h** has also the smaller size of anatase and rutile crystalline domains (4.4 and 8.7 nm, respectively), as reported in Table 2. As it is seen in Fig. 8, the most active specimens were the commercial **K7000** (25 ppm h^{-1}) and **P25** (24 ppm h^{-1}). Still, the visible PC activity of the former is attributed to the presence of aryl carboxylate species, thus discussion about **K7000** will be ignored. **Ti450/2h** PC activity was higher than that of **Ti250/8h** (*i.e.* 14 *versus* 7 ppm h^{-1}).

In the gas-solid phase regime we can safely discard (dye and LMCTC) sensitisation effects. Although the apparent E_g in **Ti250/8h** is shifted to the visible range, and it possesses the highest SSA (*cf* Table 3), it is the less effective photocatalyst. A recent investigation by Besenbacher *et al*. [35], showed that the size of the crystalline domains was more important than crystallinity in the PC degradation of phenol. A recent study by Palmisano and co-authors [102] demonstrated that increasing the size of TiO_2 nanocrystals by thermal annealing improves IPA photo-degradation by reducing the defects density in the material, thus preventing the recombination of photo-generated electron-hole pairs. Furthermore, Idriss and co-workers [27], observed higher PC H_2 generation on a catalyst composed of 80% anatase, 18% rutile and 2% brookite – this being, roughly, the composition of **P25**. Those in references [27,35] might be the reasons for the superior IPA degradation of **P25** compared to that of **Ti250/8h**, regardless of the higher SSA and smaller size of both anatase and rutile crystalline domains in the latter. Indeed, **Ti450/2h** – being a mixture of anatase (70.2 wt%), rutile (15.4 wt%), brookite (6.7 wt%) and amorphous (7.6 wt%) – showed a higher PC IPA degradation than **Ti250/8h** (14 *vs* 7 ppm h^{-1}). Additionally, we can genuinely assume that IPA, in **P25** and **Ti450/2h**, was oxidised to acetone (passing through several reaction pathways) by reaction with $^{\bullet}OH$ (created by the photo-generated h^+) and $^{\bullet}O_2^-$ [103,104]. This proviso looking at the experiments using scavengers in the liquid-solid phase: h^+ and $^{\bullet}O_2^-$ were the main oxidative species in **P25** and **Ti450/2h**. The single crystal facets of both rutile and anatase are another variable to take into account. For instance, Matsumura and

colleagues found that the {110} facets of rutile particles provides the effective reduction site and the {011} facets works as the oxidation site [105]. Other researchers proved that clean anatase {010} facets showed the highest photocatalytic reactivity in generating OH radicals and hydrogen evolution [106]. Yet others demonstrated that the photo-oxidation activity of {001} facets is greater than that of {101} facets when the crystals size of anatase TiO_2 is identical [107]. Therefore, a synergistic effect on the PC activity of those exposed anatase and rutile facets cannot be excluded *a priori*.

To further investigate the scenario under visible-light irradiation, PL spectra (displayed in Fig. 9) were recorded with λ_{ex} = 604 nm. In them, the broad band centred at around 420 nm is assigned to Ti^{4+} in octahedral coordination; the emissions at higher wavelength are attributed to the recombination of charge carriers [108]. The recombination of the photo-generated pair lead PL emission, thus a decrease in the PL signal indicates less e^-/h^+ recombination. **P25** possesses the lowest PL signal, followed by **Ti450/2h**, with **Ti250/8h** having that most intense. This means that the recombination rate of the photo-generated pair is lower in **P25**, and higher in **Ti250/8h**, being perfectly consistent with gas-solid phase PC results. Therefore, in **P25** (and to a lesser extent in **Ti450/2h**), a proposed path of the excited electron is described in Scheme 1b. When an anatase-rutile junction is excited by visible-light, an electron transfers itself from the VB to the CB of the rutile TiO_2 polymorph, leaving a hole behind [path (1) in Scheme 1b]. That hole is able to generate $^{\bullet}OH$ radicals. The electron, on the other hand, migrates to the less negative CB of anatase, generating $^{\bullet}O_2^-$ by reaction with adsorbed oxygen [path (2) in Scheme 1b]. This enables an efficient separation of the charge carriers.

At last, results reported in this work emphasise once more the complexity of PC water and air purification processes on anatase-rutile mixed phases, when adopting a visible-light source. From one hand, in the liquid-solid phase, visible-light dye and LMCTC sensitisation effects (favoured by a high surface hydroxylation) seem to dictate the disappearance of RhB and 4-CP, respectively. Still, in the gas-solid phase, it appears that anatase and rutile together are needed for inducing absorption of visible-light, and also for an efficient separation of photo-generated charge carriers, as shown in Fig. 9 and Scheme 1b.

4. Conclusions

The real crystalline and amorphous composition of three synthesised TiO_2, as well as that of three commercially available photocatalytic nano-TiO_2 (chosen because they are most widely used in the catalytic community), were investigated in very detail. This was done *via* an advanced X-ray method, the Rietveld-RIR method. The microstructure of the specimens was also studied thru an advanced X-ray method, namely the whole powder pattern modelling, quite rare indeed among the catalysis community. The results obtained by these two methods were confirmed by using advanced transmission electron microscopy

techniques. In particular, high-resolution electron energy-loss spectroscopy was used to check the homogeneity of the local chemical environment at the nanoscale.

Results showed that a hetero-junction made by a combination of anatase and rutile nanoparticles, thermally treated at a relatively low temperature (*i.e.* 250 °C), having average diameters below 10 nm (thus having high specific surface area, and also adsorbing water from the atmosphere), with an absolute rutile fraction as small as 2 wt%, is able to red-shift the apparent optical band gap of the hetero-structure, and to harvest visible-light. These features together seemed to dictate its visible-light induced photocatalytic activity, in the liquid-solid phase (RhB and 4-CP). It was also shown that, under these experimental conditions, amorphous fraction had no relevant influence on the visible-light induced photocatalytic activity. All in all, in the liquid-solid phase we assisted to dye and LMCTC sensitisations more than a purely photocatalytic process – *i.e.* photo-oxidation by direct TiO_2 excitation.

In the gas-solid phase regime (IPA degradation), on the other hand, neither dye nor LMCTC sensitisation effects are known to be granted. Under these experimental conditions, both anatase and rutile are still required for harvesting visible-light and for effective charge carrier separation. Still, a rutile weight content higher than 2 wt% (*i.e.* around 10 wt%, as in **P25**) as well as bigger size of the crystalline domains (*i.e.* samples calcined at temperature higher than 250 °C: less defects density in the material), together with a lower rate in the recombination of the photo-generated charge carriers, were shown to be more effective for a real (*i.e.* direct TiO_2 excitation) IPA photocatalytic oxidation.

Acknowledgements

This work was developed within the scope of the project CICECO-Aveiro Institute of Materials, FCT Ref. UID/CTM/50011/2019, financed by national funds through the FCT/MCTES. David Maria Tobaldi is grateful to Portuguese national funds (OE), through FCT, I.P., in the scope of the framework contract foreseen in the numbers 4, 5 and 6 of the article 23, of the Decree-Law 57/2016, of August 29, changed by Law 57/2017, of July 19. We are obliged to Prof J Tedim and Prof LD Carlos (DEMaC/CICECO–Aveiro Institute of Materials and Physics Department and CICECO–Aveiro Institute of Materials, University of Aveiro, Portugal) for their constructive and fruitful discussions that improved the manuscript noticeably. The STEM and EELS measurements were performed in the Laboratorio de Microscopias Avanzadas (LMA) at the Instituto de Nanociencia de Aragon (INA) – Universidad de Zaragoza (Spain). R.A. gratefully acknowledges the support from the Spanish Ministerio de Economia y Competitividad (MAT2016-79776-P), from the Government of Aragon and the European Social Fund under the project “Construyendo Europa desde Aragon” 2014-2020 (grant number E/26). We also acknowledge financial support from the Slovenian Research Agency through the research programme No. P2-0273. Miss Dafne M Glaglanon is kindly acknowledged for proof-editing the English of the manuscript.

References

[1] A. Fujishima, K. Honda, Electrochemical Photolysis of Water at a Semiconductor Electrode, Nature. 238 (1972) 37–38. doi:10.1038/238037a0.

[2] P.V. Kamat, A Conversation with Akira Fujishima, ACS Energy Lett. 2 (2017) 1586–1587. doi:10.1021/acsenergylett.7b00483.

[3] X. Chen, A. Selloni, Introduction: Titanium Dioxide (TiO_2) Nanomaterials, Chem. Rev. 114 (2014) 9281–9282. doi:10.1021/cr500422r.

[4] H. Zhang, J.F. Banfield, Structural Characteristics and Mechanical and Thermodynamic Properties of Nanocrystalline TiO $_2$, Chem. Rev. 114 (2014) 9613–9644. doi:10.1021/cr500072j.

[5] T. Luttrell, S. Halpegamage, J. Tao, A. Kramer, E. Sutter, M. Batzill, Why is anatase a better photocatalyst than rutile? - Model studies on epitaxial TiO2 films, Sci. Rep. 4 (2014) 4043. doi:10.1038/srep04043.

[6] G. Odling, N. Robertson, Why is Anatase a Better Photocatalyst than Rutile? The Importance of Free Hydroxyl Radicals, ChemSusChem. 8 (2015) 1838–1840. doi:10.1002/cssc.201500298.

[7] S.-D. Mo, W.Y. Ching, Electronic and optical properties of three phases of titanium dioxide: Rutile, anatase, and brookite, Phys. Rev. B. 51 (1995) 13023–13032. doi:10.1103/PhysRevB.51.13023.

[8] Z. Şen, Solar energy fundamentals and modeling techniques: atmosphere, environment, climate change, and renewable energy, Springer, London, 2008.

[9] V. Etacheri, C. Di Valentin, J. Schneider, D. Bahnemann, S.C. Pillai, Visible-light activation of TiO2 photocatalysts: Advances in theory and experiments, J. Photochem. Photobiol. C Photochem. Rev. 25 (2015) 1–29. doi:10.1016/j.jphotochemrev.2015.08.003.

[10] M. Anpo, Use of visible light. Second-generation titanium oxide photocatalysts prepared by the application of an advanced metal ion-implantation method, Pure Appl. Chem. 72 (2000) 1787–1792. doi:10.1351/pac200072091787.

[11] J.-M. Herrmann, Detrimental cationic doping of titania in photocatalysis: why chromium Cr3+-doping is a catastrophe for photocatalysis, both under UV- and visible irradiations, New J. Chem. 36 (2012) 883–890. doi:10.1039/C2NJ20914D.

[12] J. Wang, P. Zhang, X. Li, J. Zhu, H. Li, Synchronical pollutant degradation and H2 production on a Ti3+-doped TiO_2 visible photocatalyst with dominant (0 0 1) facets, Appl. Catal. B Environ. 134–135 (2013) 198–204. doi:10.1016/j.apcatb.2013.01.006.

[13] Y. Zhou, C. Chen, N. Wang, Y. Li, H. Ding, Stable Ti3+ Self-Doped Anatase-Rutile Mixed TiO2 with Enhanced Visible Light Utilization and Durability, J. Phys. Chem. C. 120 (2016) 6116–6124. doi:10.1021/acs.jpcc.6b00655.

[14] D. Ravelli, D. Dondi, M. Fagnoni, A. Albini, Photocatalysis. A multi-faceted concept for green chemistry, Chem. Soc. Rev. 38 (2009) 1999–2011. doi:10.1039/B714786B.

[15] R. Asahi, T. Morikawa, T. Ohwaki, K. Aoki, Y. Taga, Visible-Light Photocatalysis in Nitrogen-Doped Titanium Oxides, Science. 293 (2001) 269–271. doi:10.1126/science.1061051.

[16] J.-M. Herrmann, Photocatalysis fundamentals revisited to avoid several misconceptions, Appl. Catal. B Environ. 99 (2010) 461–468. doi:10.1016/j.apcatb.2010.05.012.

[17] D.M. Tobaldi, R.C. Pullar, A.F. Gualtieri, G. Otero-Irurueta, M.K. Singh, M.P. Seabra, J.A. Labrincha, Nitrogen-modified nano-titania: True phase composition, microstructure and visible-light induced photocatalytic NO_x abatement, J. Solid State Chem. 231 (2015) 87–100. doi:10.1016/j.jssc.2015.08.008.

[18] H. Saito, Y. Nosaka, Mechanism of Singlet Oxygen Generation in Visible-Light-Induced Photocatalysis of Gold-Nanoparticle-Deposited Titanium Dioxide, J. Phys. Chem. C. 118 (2014) 15656–15663. doi:10.1021/jp502440f.

[19] A. Sousa-Castillo, M. Comesaña-Hermo, B. Rodríguez-González, M. Pérez-Lorenzo, Z. Wang, X.-T. Kong, A.O. Govorov, M.A. Correa-Duarte, Boosting Hot Electron-Driven Photocatalysis through Anisotropic Plasmonic Nanoparticles with Hot Spots in Au–TiO2 Nanoarchitectures, J. Phys. Chem. C. 120 (2016) 11690–11699. doi:10.1021/acs.jpcc.6b02370.

[20] M.J. Hernández Rodríguez, E. Pulido Melián, D. García Santiago, O. González Díaz, J.A. Navío, J.M. Doña Rodríguez, NO photooxidation with TiO2 photocatalysts modified with gold and platinum, Appl. Catal. B Environ. 205 (2017) 148–157. doi:10.1016/j.apcatb.2016.12.006.
[21] M. Karmaoui, L. Lajaunie, D.M. Tobaldi, G. Leonardi, C. Benbayer, R. Arenal, J.A. Labrincha, G. Neri, Modification of anatase using noble-metals (Au, Pt, Ag): Toward a nanoheterojunction exhibiting simultaneously photocatalytic activity and plasmonic gas sensing, Appl. Catal. B Environ. 218 (2017) 370–384. doi:10.1016/j.apcatb.2017.06.010.
[22] M. Mattesini, J. Almeida, L. Dubrovinsky, N. Dubrovinskaia, B. Johansson, R. Ahuja, Cubic TiO2 As a Potential Light Absorber in Solar-Energy Conversion, Phys Rev B. 70 (2004). doi:10.1103/PhysRevB.70.115101.
[23] D.Y. Kim, J.S. de Almeida, L. Koči, R. Ahuja, Dynamical stability of the hardest known oxide and the cubic solar material: TiO2, Appl. Phys. Lett. 90 (2007) 171903. doi:10.1063/1.2731522.
[24] D.M. Tobaldi, R.C. Pullar, M.P. Seabra, J.A. Labrincha, Fully quantitative X-ray characterisation of Evonik Aeroxide TiO2 P25®, Mater. Lett. 122 (2014) 345–347. doi:10.1016/j.matlet.2014.02.055.
[25] D.C. Hurum, A.G. Agrios, K.A. Gray, T. Rajh, M.C. Thurnauer, Explaining the Enhanced Photocatalytic Activity of Degussa P25 Mixed-Phase TiO2 Using EPR, J. Phys. Chem. B. 107 (2003) 4545–4549. doi:10.1021/jp0273934.
[26] C. Maheu, L. Cardenas, E. Puzenat, P. Afanasiev, C. Geantet, UPS and UV spectroscopies combined to position the energy levels of TiO2 anatase and rutile nanopowders, Phys. Chem. Chem. Phys. 20 (2018) 25629–25637. doi:10.1039/C8CP04614J.
[27] A.K. Wahab, S. Ould-Chikh, K. Meyer, H. Idriss, On the “possible” synergism of the different phases of TiO2 in photo-catalysis for hydrogen production, J. Catal. 352 (2017) 657–671. doi:10.1016/j.jcat.2017.04.033.
[28] M. Nolan, N.Aaron. Deskins, K.C. Schwartzenberg, K.A. Gray, Local Interfacial Structure Influences Charge Localization in Titania Composites: Beyond the Band Alignment Paradigm, J. Phys. Chem. C. 120 (2016) 1808–1815. doi:10.1021/acs.jpcc.5b12326.
[29] D.O. Scanlon, C.W. Dunnill, J. Buckeridge, S.A. Shevlin, A.J. Logsdail, S.M. Woodley, C.R.A. Catlow, M.J. Powell, R.G. Palgrave, I.P. Parkin, G.W. Watson, T.W. Keal, P. Sherwood, A. Walsh, A.A. Sokol, Band alignment of rutile and anatase TiO2, Nat. Mater. 12 (2013) 798–801. doi:10.1038/nmat3697.
[30] Y. Nosaka, A.Y. Nosaka, Reconsideration of Intrinsic Band Alignments within Anatase and Rutile TiO2, J. Phys. Chem. Lett. 7 (2016) 431–434. doi:10.1021/acs.jpclett.5b02804.
[31] J. Buckeridge, K.T. Butler, C.R.A. Catlow, A.J. Logsdail, D.O. Scanlon, S.A. Shevlin, S.M. Woodley, A.A. Sokol, A. Walsh, Polymorph Engineering of TiO2: Demonstrating How Absolute Reference Potentials Are Determined by Local Coordination, Chem. Mater. 27 (2015) 3844–3851. doi:10.1021/acs.chemmater.5b00230.
[32] T. van der Meulen, A. Mattson, L. Österlund, A comparative study of the photocatalytic oxidation of propane on anatase, rutile, and mixed-phase anatase–rutile TiO2 nanoparticles: Role of surface intermediates, J. Catal. 251 (2007) 131–144. doi:10.1016/j.jcat.2007.07.002.
[33] H. Jensen, K.D. Joensen, J.-E. Jørgensen, J.S. Pedersen, G. Søgaard, Characterization of nanosized partly crystalline photocatalysts, J. Nanoparticle Res. 6 (2004) 519–526. doi:10.1007/s11051-004-1714-3.
[34] G. Bertoni, E. Beyers, J. Verbeeck, M. Mertens, P. Cool, E.F. Vansant, G. Van Tendeloo, Quantification of crystalline and amorphous content in porous TiO2 samples from electron energy loss spectroscopy, Ultramicroscopy. 106 (2006) 630–635. doi:10.1016/j.ultramic.2006.03.006.
[35] X. Wang, L. Sø, R. Su, S. Wendt, P. Hald, A. Mamakhel, C. Yang, Y. Huang, B.B. Iversen, F. Besenbacher, The influence of crystallite size and crystallinity of anatase nanoparticles on the photo-degradation of phenol, J. Catal. 310 (2014) 100–108. doi:10.1016/j.jcat.2013.04.022.
[36] V.A. Lebedev, D.A. Kozlov, I.V. Kolesnik, A.S. Poluboyarinov, A.E. Becerikli, W. Grünert, A.V. Garshev, The amorphous phase in titania and its influence on photocatalytic properties, Appl. Catal. B Environ. 195 (2016) 39–47. doi:10.1016/j.apcatb.2016.05.010.

[37] M. Bellardita, A. Di Paola, B. Megna, L. Palmisano, Absolute crystallinity and photocatalytic activity of brookite TiO2 samples, Appl. Catal. B Environ. 201 (2017) 150–158. doi:10.1016/j.apcatb.2016.08.012.
[38] J. Soria, J. Sanz, M.J. Torralvo, I. Sobrados, C. Garlisi, G. Palmisano, S. Çetinkaya, S. Yurdakal, V. Augugliaro, The effect of the surface disordered layer on the photoreactivity of titania nanoparticles, Appl. Catal. B Environ. 210 (2017) 306–319. doi:10.1016/j.apcatb.2017.03.045.
[39] B. Ohtani, Y. Ogawa, S. Nishimoto, Photocatalytic Activity of Amorphous−Anatase Mixture of Titanium(IV) Oxide Particles Suspended in Aqueous Solutions, J. Phys. Chem. B. 101 (1997) 3746–3752. doi:10.1021/jp962702+.
[40] M. Pera-Titus, V. García-Molina, M.A. Baños, J. Giménez, S. Esplugas, Degradation of chlorophenols by means of advanced oxidation processes: a general review, Appl. Catal. B Environ. 47 (2004) 219–256. doi:10.1016/j.apcatb.2003.09.010.
[41] D.M. Tobaldi, R.C. Pullar, A.F. Gualtieri, M.P. Seabra, J.A. Labrincha, Sol–gel synthesis, characterisation and photocatalytic activity of pure, W-, Ag- and W/Ag co-doped TiO2 nanopowders, Chem. Eng. J. 214 (2013) 364–375. doi:10.1016/j.cej.2012.11.018.
[42] D.M. Tobaldi, M.P. Seabra, G. Otero-Irurueta, Y.R. de Miguel, R.J. Ball, M.K. Singh, R.C. Pullar, J.A. Labrincha, Quantitative XRD characterisation and gas-phase photocatalytic activity testing for visible-light (indoor applications) of KRONOClean 7000®, RSC Adv. 5 (2015) 102911–102918. doi:10.1039/C5RA22816F.
[43] A.F. Gualtieri, Accuracy of XRPD QPA using the combined Rietveld-RIR method, J. Appl. Crystallogr. 33 (2000) 267–278. doi:10.1107/S002188989901643X.
[44] A.F. Gualtieri, G. Brignoli, Rapid and accurate quantitative phase analysis using a fast detector, J. Appl. Crystallogr. 37 (2004) 8–13. doi:10.1107/S0021889803022052.
[45] J.P. Cline, R.B. Von Dreele, R. Winburn, P.W. Stephens, J.J. Filliben, Addressing the amorphous content issue in quantitative phase analysis: the certification of NIST standard reference material 676a, Acta Crystallogr. A. 67 (2011) 357–367. doi:10.1107/S0108767311014565.
[46] I.C. Madsen, N.V.Y. Scarlett, Chapter 11. Quantitative Phase Analysis, in: R.E. Dinnebier, S.J.L. Billinge (Eds.), Powder Diffr., Royal Society of Chemistry, Cambridge, 2008: pp. 298–331. http://ebook.rsc.org/?DOI=10.1039/9781847558237-00298.
[47] A.C. Larson, R.B. Von Dreele, General Structure Analysis System (GSAS), Los Alamos National Laboratory Report LAUR, 2004.
[48] B.H. Toby, EXPGUI, a graphical user interface for GSAS, J. Appl. Crystallogr. 34 (2001) 210–213. doi:10.1107/S0021889801002242.
[49] P. Thompson, D.E. Cox, J.B. Hastings, Rietveld refinement of Debye–Scherrer synchrotron X-ray data from Al_2O_3, J. Appl. Crystallogr. 20 (1987) 79–83. doi:10.1107/S0021889887087090.
[50] C.J. Howard, T.M. Sabine, F. Dickson, Structural and thermal parameters for rutile and anatase, Acta Crystallogr. B. 47 (1991) 462–468. doi:10.1107/S010876819100335X.
[51] E.P. Meagher, G.A. Lager, Polyhedral thermal expansion in the TiO2 polymorphs; refinement of the crystal structures of rutile and brookite at high temperature, Can Miner. 17 (1979) 77–85.
[52] D.M. Tobaldi, R.C. Pullar, A.F. Gualtieri, M.P. Seabra, J.A. Labrincha, Phase composition, crystal structure and microstructure of silver and tungsten doped TiO2 nanopowders with tuneable photochromic behaviour, Acta Mater. 61 (2013) 5571–5585. doi:10.1016/j.actamat.2013.05.041.
[53] P. Scardi, M. Leoni, Whole powder pattern modelling, Acta Crystallogr. A. 58 (2002) 190–200. doi:10.1107/S0108767301021298.
[54] P. Scardi, M. Leoni, Whole Powder Pattern Modelling: Theory and Applications, in: Diffr. Anal. Microstruct. Mater., Springer-Verlag, Eric J. Mittemeijer, Paolo Scardi, Berlin, 2004: pp. 51–92.
[55] M. Leoni, T. Confente, P. Scardi, PM2K: a flexible program implementing Whole Powder Pattern Modelling, Z. Für Krist. Suppl. 23 (2006) 249–254. doi:10.1524/zksu.2006.suppl_23.249.
[56] P. Scardi, M. Leoni, Line profile analysis: pattern modelling versus profile fitting, J. Appl. Crystallogr. 39 (2006) 24–31. doi:10.1107/S0021889805032978.
[57] P. Scardi, M. Ortolani, M. Leoni, WPPM: Microstructural Analysis beyond the Rietveld Method, Mater. Sci. Forum. 651 (2010) 155–171. doi:10.4028/www.scientific.net/MSF.651.155.

[58] M. Karmaoui, E.V. Ramana, D.M. Tobaldi, L. Lajaunie, M.P. Graça, R. Arenal, M.P. Seabra, J.A. Labrincha, R.C. Pullar, High dielectric constant and capacitance in ultrasmall (2.5 nm) SrHfO3 perovskite nanoparticles produced in a low temperature non-aqueous sol–gel route, RSC Adv. 6 (2016) 51493–51502. doi:10.1039/C6RA06990H.
[59] M. Karmaoui, J.S. Amaral, L. Lajaunie, H. Puliyalil, D.M. Tobaldi, R.C. Pullar, J.A. Labrincha, R. Arenal, U. Cvelbar, Smallest Bimetallic CoPt3 Superparamagnetic Nanoparticles, J. Phys. Chem. Lett. 7 (2016) 4039–4046. doi:10.1021/acs.jpclett.6b01768.
[60] H.P. Klug, L.E. Alexander, X-ray diffraction procedures for polycrystalline and amorphous materials, 2nd Edition, Wiley, New York, 1974.
[61] G.K. Williamson, W.H. Hall, X-ray line broadening from filed aluminium and wolfram, Acta Metall. 1 (1953) 22–31. doi:10.1016/0001-6160(53)90006-6.
[62] B.E. Warren, X-ray Diffraction, Courier Corporation, 1969.
[63] C. Weidenthaler, Pitfalls in the characterization of nanoporous and nanosized materials, Nanoscale. 3 (2011) 792–810. doi:10.1039/C0NR00561D.
[64] G. Caglioti, A. Paoletti, F.P. Ricci, On resolution and luminosity of a neutron diffraction spectrometer for single crystal analysis, Nucl. Instrum. Methods. 9 (1960) 195–198. doi:10.1016/0029-554X(60)90101-4.
[65] P. Stadelmann, JEMS-SAAS, (2014).
[66] Hyperspy: Multidimensional data analysis, HyperSpy, 2017. https://github.com/hyperspy/hyperspy.
[67] A. Dolgonos, T.O. Mason, K.R. Poeppelmeier, Direct optical band gap measurement in polycrystalline semiconductors: A critical look at the Tauc method, J. Solid State Chem. 240 (2016) 43–48. doi:10.1016/j.jssc.2016.05.010.
[68] D.M. Tobaldi, R.C. Pullar, L. Durães, T. Matias, M.P. Seabra, J.A. Labrincha, Truncated tetragonal bipyramidal anatase nanocrystals formed without use of capping agents from the supercritical drying of a TiO_2 sol, CrystEngComm. 18 (2016) 164–176. doi:10.1039/C5CE02112J.
[69] R.G. Burns, Mineralogical Applications of Crystal Field Theory, Cambridge University Press, 1993.
[70] D.M. Tobaldi, A. Tucci, A.S. Škapin, L. Esposito, Effects of SiO2 addition on TiO2 crystal structure and photocatalytic activity, J. Eur. Ceram. Soc. 30 (2010) 2481–2490. doi:10.1016/j.jeurceramsoc.2010.05.014.
[71] M. Tasbihi, U.L. Štangar, A.S. Škapin, A. Ristić, V. Kaučič, N.N. Tušar, Titania-containing mesoporous silica powders: Structural properties and photocatalytic activity towards isopropanol degradation, J. Photochem. Photobiol. Chem. 216 (2010) 167–178. doi:10.1016/j.jphotochem.2010.07.011.
[72] D.M. Tobaldi, C. Piccirillo, N. Rozman, R.C. Pullar, M.P. Seabra, A.S. Škapin, P.M. Castro, J.A. Labrincha, Effects of Cu, Zn and Cu-Zn addition on the microstructure and antibacterial and photocatalytic functional properties of Cu-Zn modified TiO2 nano-heterostructures, J. Photochem. Photobiol. Chem. 330 (2016) 44–54.
[73] R.I. Bickley, G. Munuera, F.S. Stone, Photoadsorption and photocatalysis at rutile surfaces: II. Photocatalytic oxidation of isopropanol, J. Catal. 31 (1973) 398–407. doi:10.1016/0021-9517(73)90311-4.
[74] G. Munuera, F. Moreno, J.A. Prieto, Temperature Programmed Desorption of Water Adsorbed on Anatase Surfaces, Z. Für Phys. Chem. 78 (2011) 113–117. doi:10.1524/zpch.1972.78.3_4.113.
[75] S. Larson, J.A. Widegren, J.L. Falconer, Transient Studies of 2-Propanol Photocatalytic Oxidation on Titania, J. Catal. 157 (1995) 611–625. doi:10.1006/jcat.1995.1326.
[76] Electron Energy-Loss Spectroscopy in the Electron Microscope | R.F. Egerton | Springer, n.d. //www.springer.com/gp/book/9781441995827.
[77] K. Gross, J.J.P. Barragán, S. Sangiao, J.M.D. Teresa, L. Lajaunie, R. Arenal, H.A. Calderón, P. Prieto, Electrical conductivity of oxidized-graphenic nanoplatelets obtained from bamboo: effect of the oxygen content, Nanotechnology. 27 (2016) 365708. doi:10.1088/0957-4484/27/36/365708.
[78] L. Lajaunie, C. Pardanaud, C. Martin, P. Puech, C. Hu, M.J. Biggs, R. Arenal, Advanced spectroscopic analyses on a:C-H materials: Revisiting the EELS characterization and its coupling with multi-wavelength Raman spectroscopy, Carbon. 112 (2017) 149–161. doi:10.1016/j.carbon.2016.10.092.

[79] E.D. Hanson, L. Lajaunie, S. Hao, B.D. Myers, F. Shi, A.A. Murthy, C. Wolverton, R. Arenal, V.P. Dravid, Systematic Study of Oxygen Vacancy Tunable Transport Properties of Few-Layer MoO3−x Enabled by Vapor-Based Synthesis, Adv. Funct. Mater. 27 (2017) n/a-n/a. doi:10.1002/adfm.201605380.

[80] R. Brydson, B.G. Williams, W. Engel, H. Sauer, E. Zeitler, J.M. Thomas, Electron energy-loss spectroscopy (EELS) and the electronic structure of titanium dioxide, Solid State Commun. 64 (1987) 609–612. doi:10.1016/0038-1098(87)90792-7.

[81] J.P. Crocombette, F. Jollet, Ti 2p X-ray absorption in titanium dioxides (TiO 2): the influence of the cation site environment, J. Phys. Condens. Matter. 6 (1994) 10811. doi:10.1088/0953-8984/6/49/022.

[82] P. Krüger, Multichannel multiple scattering calculation of L 2 , 3 -edge spectra of TiO 2 and SrTiO 3 : Importance of multiplet coupling and band structure, Phys. Rev. B. 81 (2010). doi:10.1103/PhysRevB.81.125121.

[83] A. Pottier, C. Chanéac, E. Tronc, L. Mazerolles, J.-P. Jolivet, Synthesis of brookite TiO2 nanoparticles by thermolysis of TiCl4 in strongly acidic aqueous media, J. Mater. Chem. 11 (2001) 1116–1121. doi:10.1039/b100435m.

[84] Y. Hu, H.-L. Tsai, C.-L. Huang, Effect of brookite phase on the anatase–rutile transition in titania nanoparticles, J. Eur. Ceram. Soc. 23 (2003) 691–696. doi:10.1016/S0955-2219(02)00194-2.

[85] B. Ohtani, O.O. Prieto-Mahaney, D. Li, R. Abe, What is Degussa (Evonik) P25? Crystalline composition analysis, reconstruction from isolated pure particles and photocatalytic activity test, J. Photochem. Photobiol. Chem. 216 (2010) 179–182. doi:10.1016/j.jphotochem.2010.07.024.

[86] D.M. Tobaldi, R.C. Pullar, R. Binions, A. Belen Jorge, P.F. McMillan, M. Saeli, M.P. Seabra, J.A. Labrincha, Influence of sol counter-ions on the visible light induced photocatalytic behaviour of TiO2 nanoparticles, Catal. Sci. Technol. 4 (2014) 2134. doi:10.1039/c4cy00423j.

[87] M. Lindner, J. Theurich, D.W. Bahnemann, Photocatalytic degradation of organic compounds: accelerating the process efficiency, Water Sci. Technol. 35 (1997) 79–86. doi:10.1016/S0273-1223(97)00012-7.

[88] D. Chen, A.K. Ray, Photodegradation kinetics of 4-nitrophenol in TiO2 suspension, Water Res. 32 (1998) 3223–3234. doi:10.1016/S0043-1354(98)00118-3.

[89] F.C. Hawthorne, Mineralogical Society of America, eds., Spectroscopic methods in mineralogy and geology, Mineralogical Society of America, Washington, D.C., 1988.

[90] T. Zhu, S.-P. Gao, The Stability, Electronic Structure, and Optical Property of TiO2 Polymorphs, J. Phys. Chem. C. 118 (2014) 11385–11396. doi:10.1021/jp412462m.

[91] J. Zhang, P. Zhou, J. Liu, J. Yu, New understanding of the difference of photocatalytic activity among anatase, rutile and brookite TiO $_2$, Phys Chem Chem Phys. 16 (2014) 20382–20386. doi:10.1039/C4CP02201G.

[92] M. Cargnello, T. Montini, S.Y. Smolin, J.B. Priebe, J.J.D. Jaén, V.V.T. Doan-Nguyen, I.S. McKay, J.A. Schwalbe, M.-M. Pohl, T.R. Gordon, Y. Lu, J.B. Baxter, A. Brückner, P. Fornasiero, C.B. Murray, Engineering titania nanostructure to tune and improve its photocatalytic activity, Proc. Natl. Acad. Sci. (2016) 201524806. doi:10.1073/pnas.1524806113.

[93] R. Kaplan, B. Erjavec, G. Dražić, J. Grdadolnik, A. Pintar, Simple synthesis of anatase/rutile/brookite TiO2 nanocomposite with superior mineralization potential for photocatalytic degradation of water pollutants, Appl. Catal. B Environ. 181 (2016) 465–474. doi:10.1016/j.apcatb.2015.08.027.

[94] A.M. Pennington, A.I. Okonmah, D.T. Munoz, G. Tsilomelekis, F.E. Celik, Changes in Polymorph Composition in P25-TiO2 during Pretreatment Analyzed by Differential Diffuse Reflectance Spectral Analysis, J. Phys. Chem. C. 122 (2018) 5093–5104. doi:10.1021/acs.jpcc.7b10449.

[95] X. Jiang, M. Manawan, T. Feng, R. Qian, T. Zhao, G. Zhou, F. Kong, Q. Wang, S. Dai, J.H. Pan, Anatase and rutile in evonik aeroxide P25: Heterojunctioned or individual nanoparticles?, Catal. Today. (2017). doi:10.1016/j.cattod.2017.06.010.

[96] K.A. Michalow, D. Logvinovich, A. Weidenkaff, M. Amberg, G. Fortunato, A. Heel, T. Graule, M. Rekas, Synthesis, characterization and electronic structure of nitrogen-doped TiO2 nanopowder, Catal. Today. 144 (2009) 7–12. doi:10.1016/j.cattod.2008.12.015.

[97] S. Balaji, Y. Djaoued, J. Robichaud, Phonon confinement studies in nanocrystalline anatase-TiO2 thin films by micro Raman spectroscopy, J. Raman Spectrosc. 37 (2006) 1416–1422. doi:10.1002/jrs.1566.
[98] W.F. Zhang, Y.L. He, M.S. Zhang, Z. Yin, Q. Chen, Raman scattering study on anatase TiO_2 nanocrystals, J. Phys. Appl. Phys. 33 (2000) 912–916. doi:10.1088/0022-3727/33/8/305.
[99] A. Li Bassi, D. Cattaneo, V. Russo, C.E. Bottani, E. Barborini, T. Mazza, P. Piseri, P. Milani, F.O. Ernst, K. Wegner, S.E. Pratsinis, Raman spectroscopy characterization of titania nanoparticles produced by flame pyrolysis: The influence of size and stoichiometry, J. Appl. Phys. 98 (2005) 074305. doi:doi:10.1063/1.2061894.
[100] B. Erdem, R.A. Hunsicker, G.W. Simmons, E.D. Sudol, V.L. Dimonie, M.S. El-Aasser, XPS and FTIR Surface Characterization of TiO2 Particles Used in Polymer Encapsulation, Langmuir. 17 (2001) 2664–2669. doi:10.1021/la0015213.
[101] J. Schneider, ed., Photocatalysis: fundamentals and perspectives, Royal Society of Chemistry, Cambridge, UK, 2016.
[102] C. Garlisi, G. Scandura, J. Szlachetko, S. Ahmadi, J. Sa, G. Palmisano, E-beam evaporated TiO2 and Cu-TiO2 on glass: Performance in the discoloration of methylene blue and 2-propanol oxidation, Appl. Catal. Gen. 526 (2016) 191–199. doi:10.1016/j.apcata.2016.08.022.
[103] Y. Ohko, K. Hashimoto, A. Fujishima, Kinetics of Photocatalytic Reactions under Extremely Low-Intensity UV Illumination on Titanium Dioxide Thin Films, J. Phys. Chem. A. 101 (1997) 8057–8062. doi:10.1021/jp972002k.
[104] F. Arsac, D. Bianchi, J.M. Chovelon, C. Ferronato, J.M. Herrmann, Experimental Microkinetic Approach of the Photocatalytic Oxidation of Isopropyl Alcohol on TiO2. Part 1. Surface Elementary Steps Involving Gaseous and Adsorbed C3HxO Species, J. Phys. Chem. A. 110 (2006) 4202–4212. doi:10.1021/jp055342b.
[105] T. Ohno, K. Sarukawa, M. Matsumura, Crystal faces of rutile and anatase TiO2 particles and their roles in photocatalytic reactions, New J. Chem. 26 (2002) 1167–1170. doi:10.1039/b202140d.
[106] J. Pan, G. Liu, G.Q.M. Lu, H.-M. Cheng, On the True Photoreactivity Order of {001}, {010}, and {101} Facets of Anatase TiO2 Crystals, Angew. Chem. Int. Ed. 50 (2011) 2133–2137. doi:10.1002/anie.201006057.
[107] Q. Wu, M. Liu, Z. Wu, Y. Li, L. Piao, Is Photooxidation Activity of {001} Facets Truly Lower Than That of {101} Facets for Anatase TiO_2 Crystals?, J. Phys. Chem. C. 116 (2012) 26800–26804. doi:10.1021/jp3087495.
[108] F.J. Knorr, J.L. McHale, Spectroelectrochemical Photoluminescence of Trap States of Nanocrystalline TiO2 in Aqueous Media, J. Phys. Chem. C. 117 (2013) 13654–13662. doi:10.1021/jp402264p.
[109] L. Pan, J.-J. Zou, X.-Y. Liu, X.-J. Liu, S. Wang, X. Zhang, L. Wang, Visible–Light–Induced Photodegradation of Rhodamine B over Hierarchical TiO2: Effects of Storage Period and Water-Mediated Adsorption Switch, Ind. Eng. Chem. Res. 51 (2012) 12782–12786. doi:10.1021/ie3019033.

Tables and Figures

Table 1 – Phase fraction (wt%) and confidence interval (CI) at 95% of studied specimens.

Sample	Phase composition, wt%							
	anatase	CI	rutile	CI	brookite	CI	amorphous	CI
Ti250/8h	88.5	1.9	2.0	0.7	3.4	1.6	6.0	3.9
Ti450/2h	70.2	1.8	15.4	2.2	6.7	0.5	7.6	2.6
Ti800/2h	–	–	99.0	1.4	–	–	1.0*	1.4
P25	78.6	5.7	10.7	2.6	–	–	10.6	4.2
K7000†	92.8	1.5	–	–	–	–	7.2	1.5
HK-UV100	79.1	1.5	–	–	–	–	20.9	1.5

Note: the wt% fraction of each phase was calculated as an average over three different sample preparations and data collections for each specimen (three different batches in case of the commercial photocatalysts). The Rietveld agreement factors were: $R(F^2) < 4.19\%$; $R_{wp} < 6.79\%$; $\chi^2 < 4.96$ for all the FQPA refinements.

There were 2285 observations for every refinement; the number of anatase, rutile and brookite (this latter when present) reflections was 32, 31 and 158, respectively.

† From reference [42].

* Values of amorphous phase less than 2 wt% are under the detection limit of the Rietveld-RIR method.

Table 2 – WPPM agreement factors, average diameter of the crystalline domains, and polydispersity index (PDI).

Sample	Agreement factors			Mean crystalline domain diameter (nm)			PDI		
	R_{wp} (%)	R_{exp} (%)	χ^2	anatase		rutile	anatase		rutile
Ti250/8h	3.65	3.38	1.08	4.4±0.1		8.7±1.4	0.06±0.01		0.09±0.03
Ti450/2h	4.27	2.31	1.85	11.0±0.1		16.1±0.1	0.11±0.01		0.23±0.04
Ti800/2h	3.89	2.49	1.56	–		89.4±3.7	–		0.13±0.03
P25[†]	3.19	2.07	1.54	15.5±0.3		19.3±0.6	0.18±0.01		0.29±0.06
K7000[‡*]	3.77	2.25	1.68	4.1±0.2	13.7±0.6	–	0.29±0.09	0.12±0.03	–
HK-UV100[*]	3.24	1.88	1.72	2.0±0.1	9.9±0.4	–	028±0.08	0.09±0.01	–

† From reference [24].

‡ Averaged from reference [42].

* The anatase crystalline domains in **K7000** and **HK-UV100** are described by a bimodal size distribution.

Table 3 – Apparent optical E_g, estimated according the Tauc procedure and the differential reflectance method (dR/dλ), BET specific surface area, 3 h pseudo-first-order apparent rate constant, and relative correlation coefficients for the tested samples, in case of RhB degradation in liquid–solid phase, using the LED white lamp.

Sample	Apparent optical E_g								SSA_{BET}	k'_{app}	
	Tauc plot				dR/dλ						
	Indirect		Direct		anatase		rutile				
	eV	nm	eV	nm	eV	nm	eV	nm	$m^2\ g^{-1}$	h^{-1}	R^2
Ti250/8h	3.05±0.01	406	3.31±0.01	374	3.10±0.01	400	–	–	134.4±2.1	1.698±0.053	0.995
Ti450/2h	2.99±0.01	415	3.27±0.01	379	3.08±0.01	403	–	–	45.9±0.7	0.347±0.022	0.980
Ti800/2h	2.91±0.01	426	3.07±0.01	403	–	–	3.00±0.01	413	1.6±0.2	0.023±0.001	0.993
P25	3.06±0.01	405	3.50±0.01	354	3.34±0.01	371	3.11±0.01	398	52.5±0.6	0.103±0.002	0.998

K7000	3.28±0.01	378	3.52±0.01	353	3.35±0.01	371	–	–	229.2±4.2	0.164±0.007	0.990
HK-UV100	3.28±0.01	378	3.60±0.01	345	3.31±0.01	375	–	–	278.8±4.3	0.055±0.001	0.999

Table 4 – Position and FWHM of Raman E_g mode of anatase

Sample	Anatase Raman E_g mode (cm^{-1})	
	Position	**FWHM**
Ti250/8h	149.6±0.2	24.2±1.3
Ti450/2h	145.1±0.1	15.4±0.6
P25	142.9±0.1	13.3±0.5
K7000	146.9±0.2	20.1±1.1
HK-UV100	148.8±0.2	22.1±1.3

Figures and captions

Fig. 1 – a) HR-STEEM HAADF micrograph of sample **Ti250/8h**; b) HR-STEM ABF micrograph of sample **Ti250/8h**. The inset shows the fast Fourier transform (FFT) image computed by using the area highlighted by a red square (scale bar = 10 nm^{-1}); c) STEM-HAADF micrograph of sample **Ti250/8h**. The green square highlights the area used for the SR-EELS analysis; d) EELS spectrum showing the Ti-$L_{2,3}$ edges recorded on **Ti250/8h**. The arrow highlights the feature that can be used to discriminate rutile, brookite and anatase structure.

Fig. 2 – a) HR-STEEM HAADF micrograph of sample **Ti450/2h**; b) HR-STEM ABF micrograph of sample **Ti450/2h**. The inset shows the fast Fourier transform image computed by using the area highlighted by a red square (scale bar = 10 nm^{-1}); c) STEM-HAADF micrograph of sample **Ti450/2h**. The green square highlights the area used for the SR-EELS analysis; d) EELS spectra showing the Ti-$L_{2,3}$ edges recorded on sample **Ti450/2h**.

Fig. 3 – a) XRPD patterns of synthesised specimens; b) XRPD patterns of commercial specimens. The vertical bars represent the XRPD reflections of anatase (black, JCPDS-PDF card no. 21-1272), rutile (red, JCPDS-PDF card no. 21-1276), brookite (light blue, JCPDS-PDF card no. 29-1360 – only the three most intense reflections were reported here).

Fig. 4 – Size distribution, as obtained from the WPPM modelling of: a) **Ti250/8h**; b) **Ti450/2h**; c) **Ti800/2h**.

Fig.5 – a) Bimodal size distribution for anatase (size reported in log-scale) in **HK-UV100**; b) WPPM output of the **HK-UV100** specimen. The red line represents the calculated pattern and the black open squares the measured one. The blue (upper) and dark grey (lower) continuous lines at the bottom are the difference curves between observed and calculated profiles, for the proposed bimodal and unimodal size distribution models, respectively. A magnification in the 20-35 °2θ range is shown in the inset, in order to highlight the difference in the most intense reflection, (101), of anatase.

Fig. 6 – Absorption data derived by Kubelka-Munk analysis of the DRS data.

Fig. 7 – DRS spectra of specimens **Ti250/8h** (orange line) and **P25** (black line). The plot of the first derivative of reflectance *versus* λ ($dR/d\lambda$) is shown in the inset, in order to highlight the rutile and anatase contribution to the apparent optical E_g of **P25**.

Fig. 8 – Gas-solid phase photocatalytic activity under visible-light exposure, expressed as the rate constant of the initial acetone formation.

Fig. 9 – Photoluminescence spectra under visible-light (λ_{ex} = 604 nm).

Fig. 1a-d

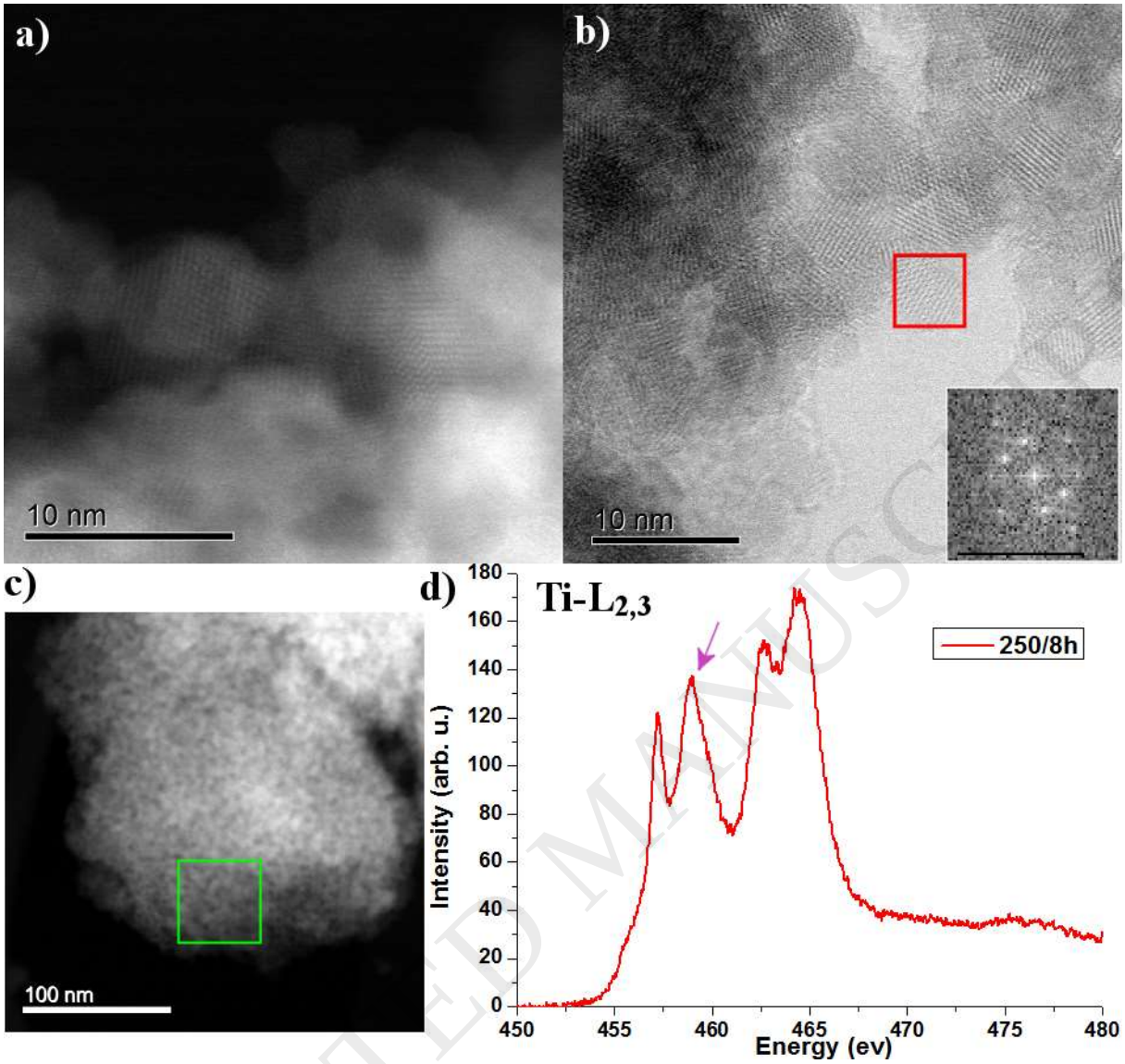

Fig. 2a-d

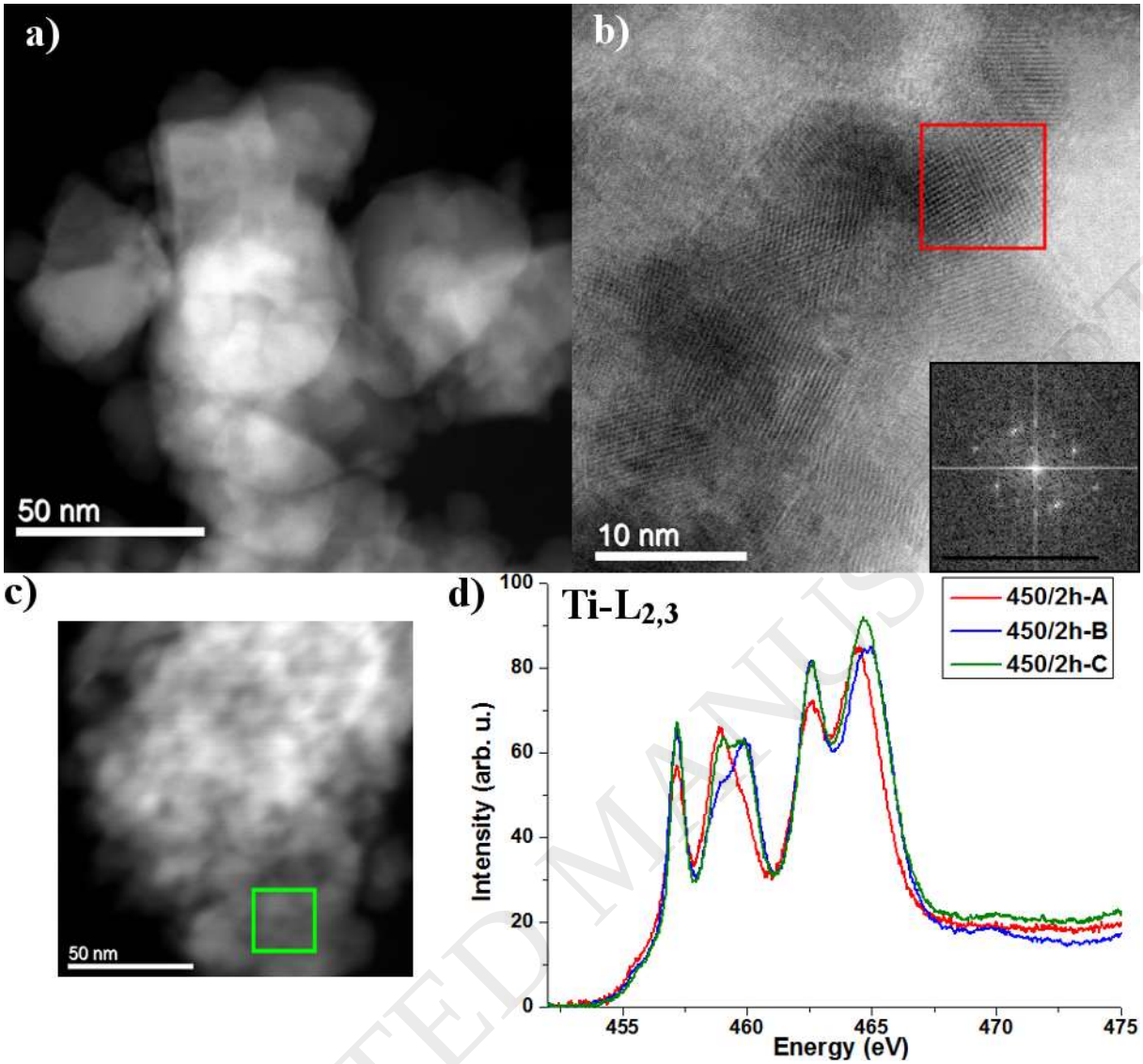

Fig. 3a

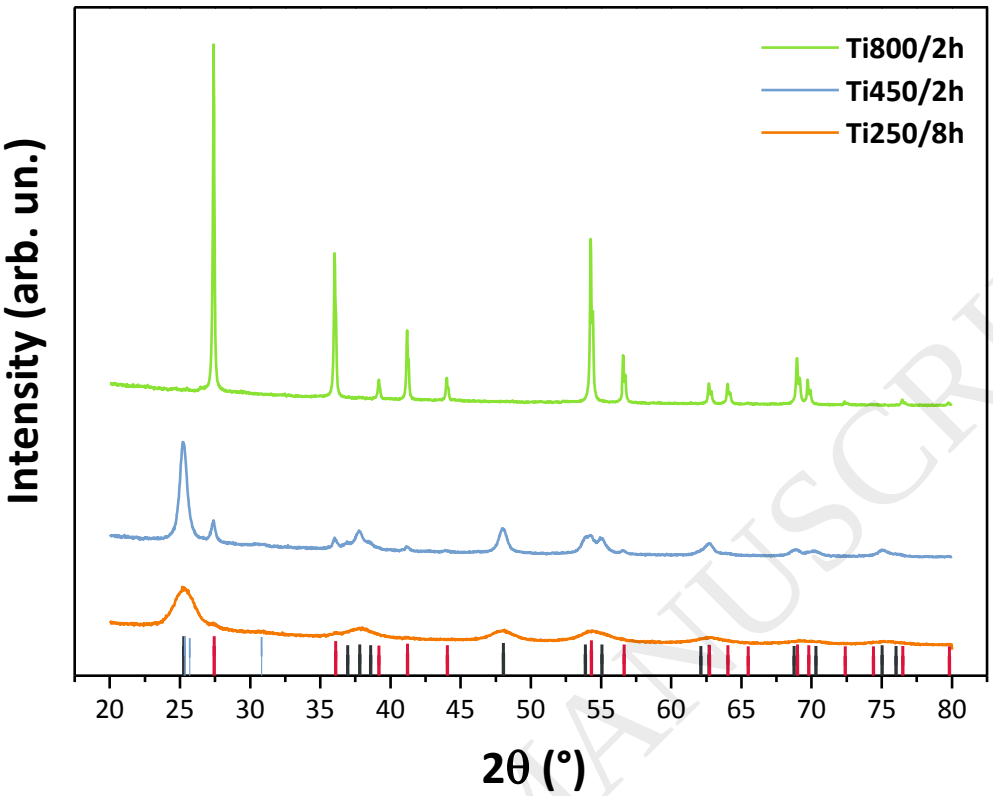

Fig. 3b

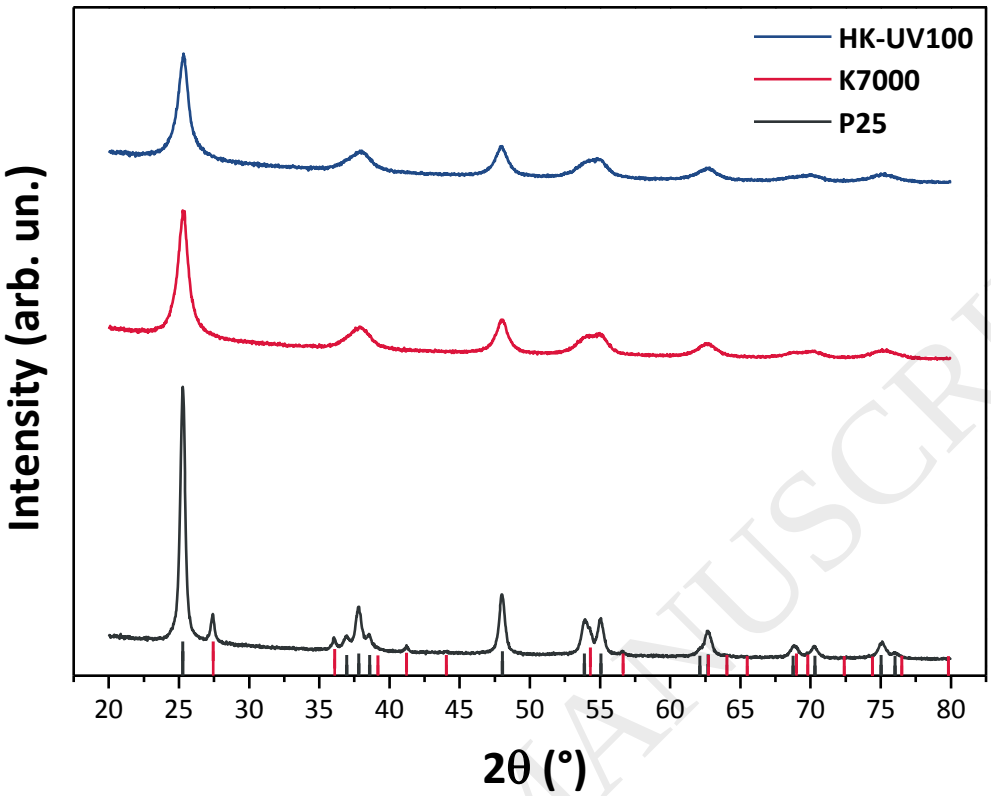

Fig. 4a

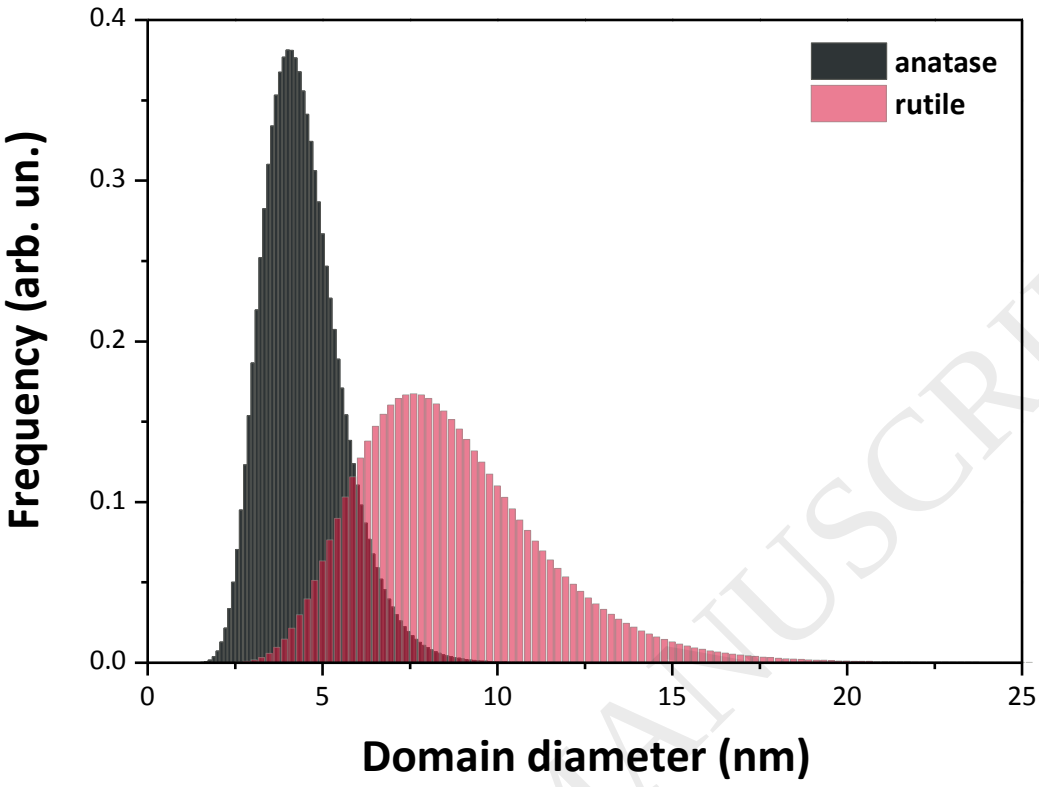

Fig. 4b

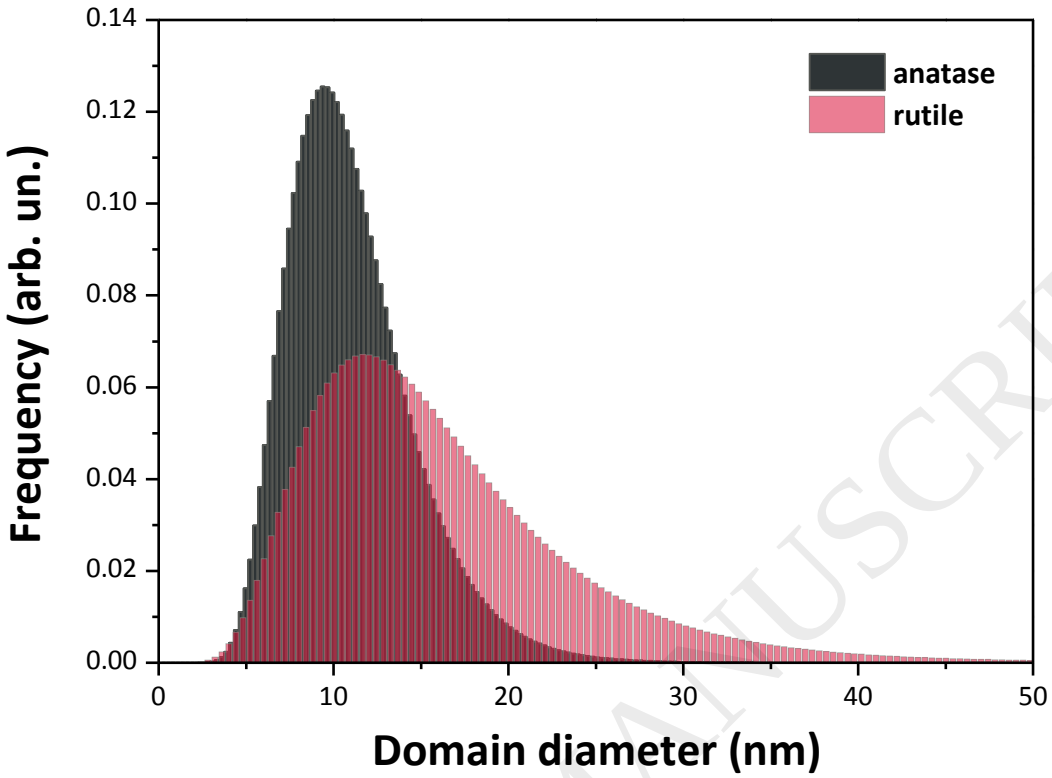

Fig. 4c

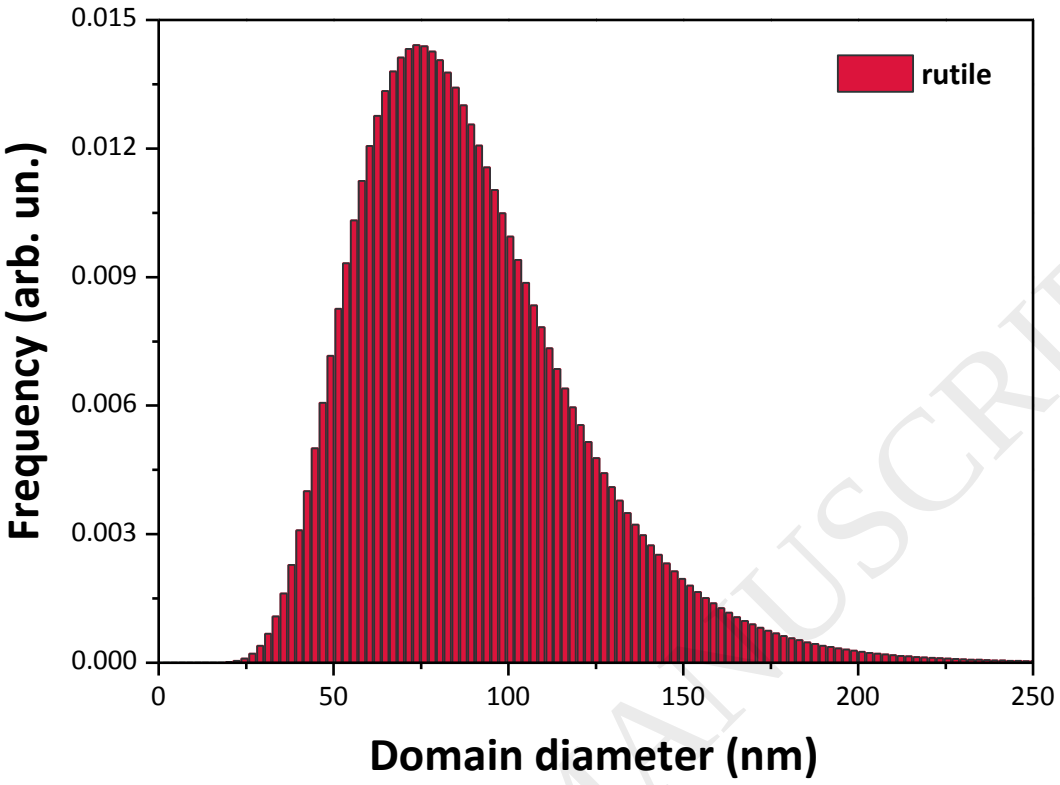

Fig. 5a

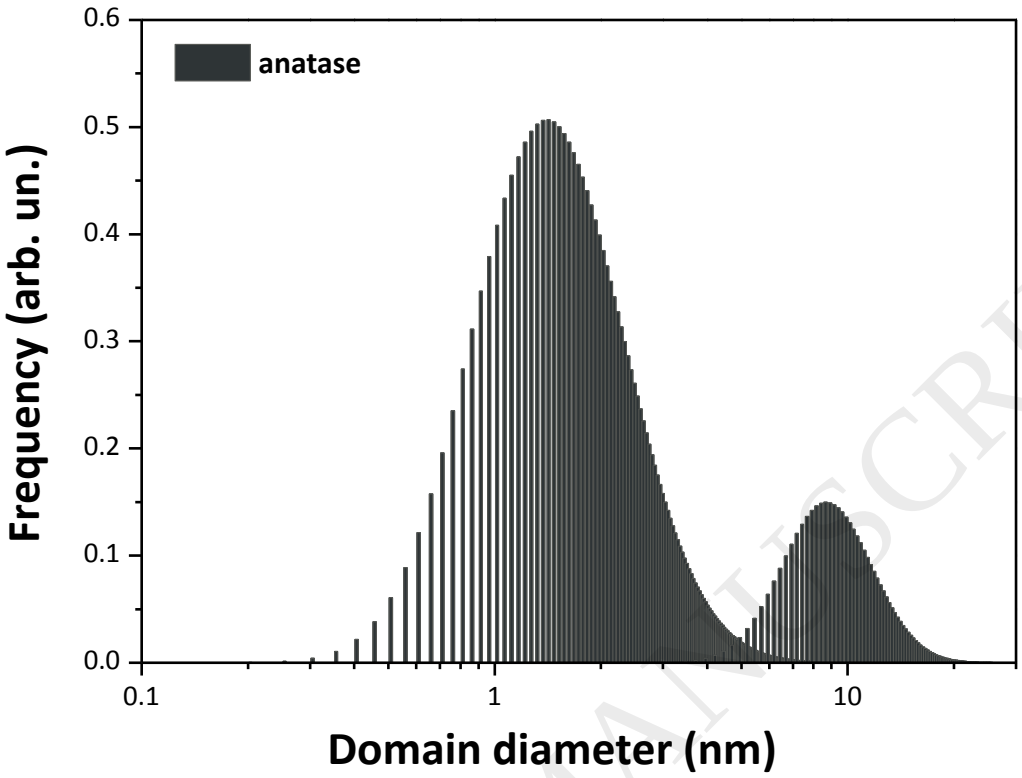

Fig. 5b

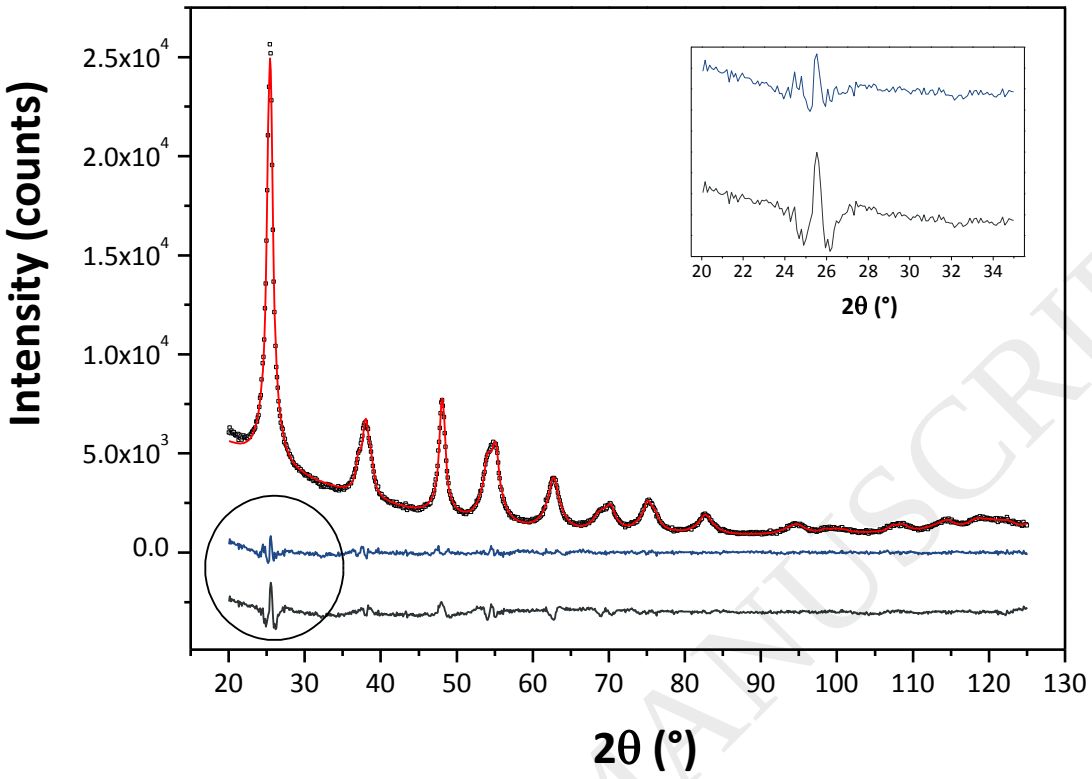

Fig. 6

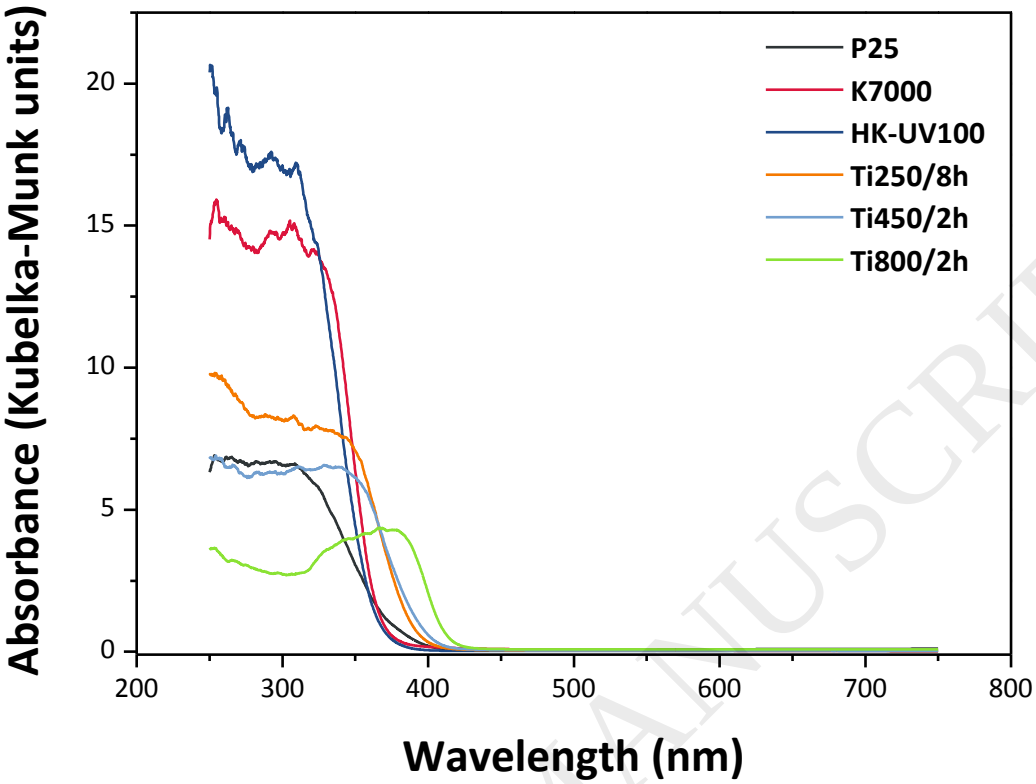

Fig. 7

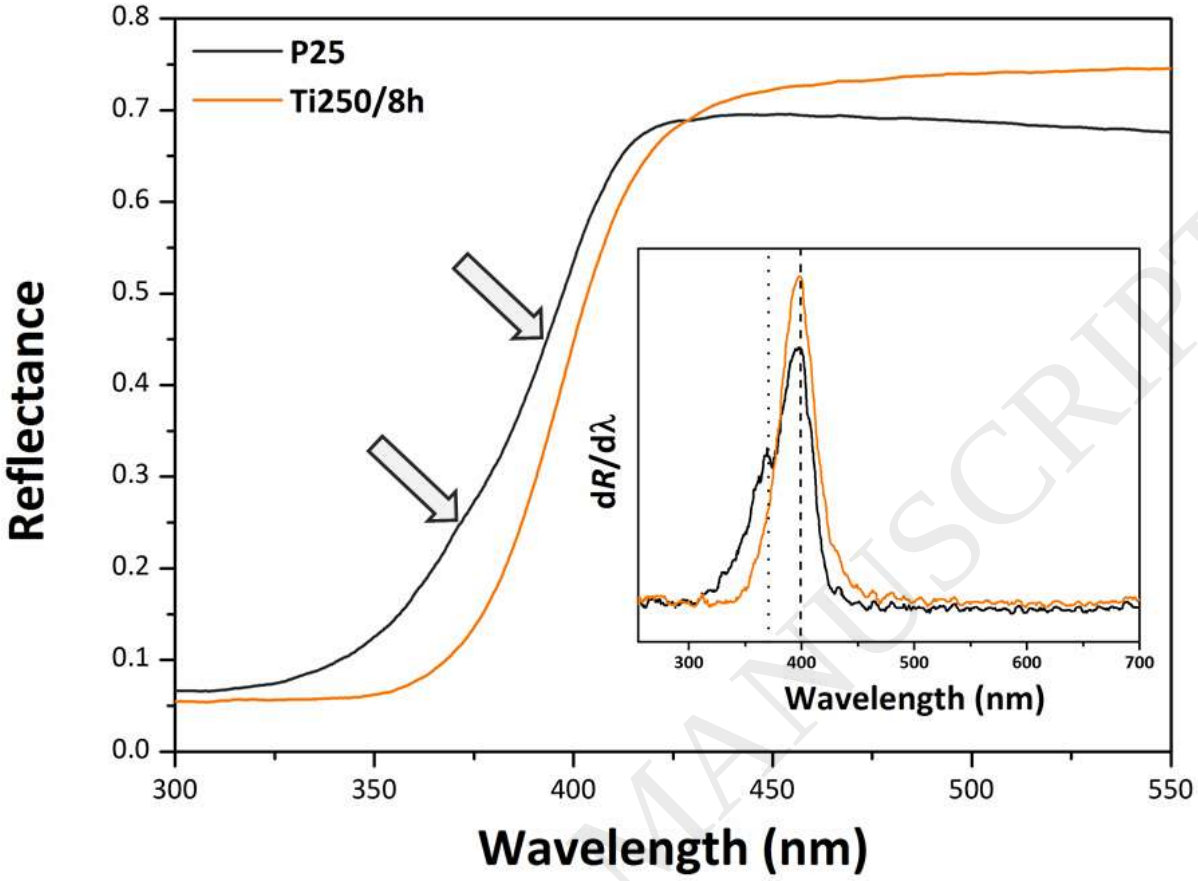

Fig. 8

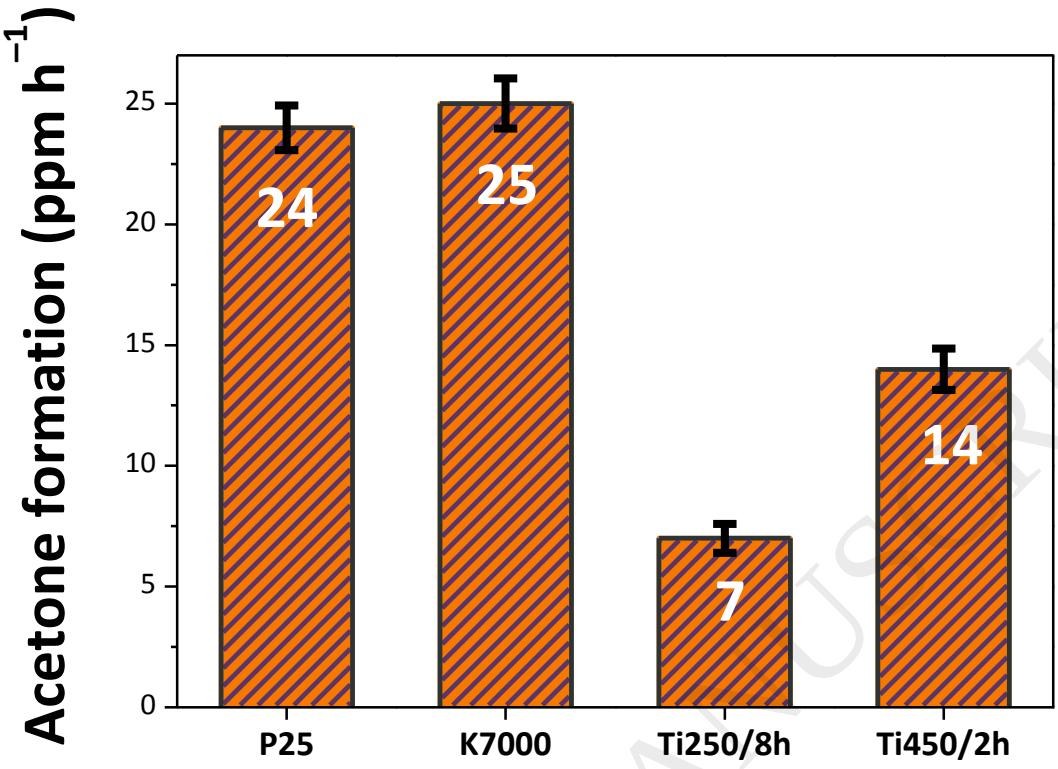

Fig. 9

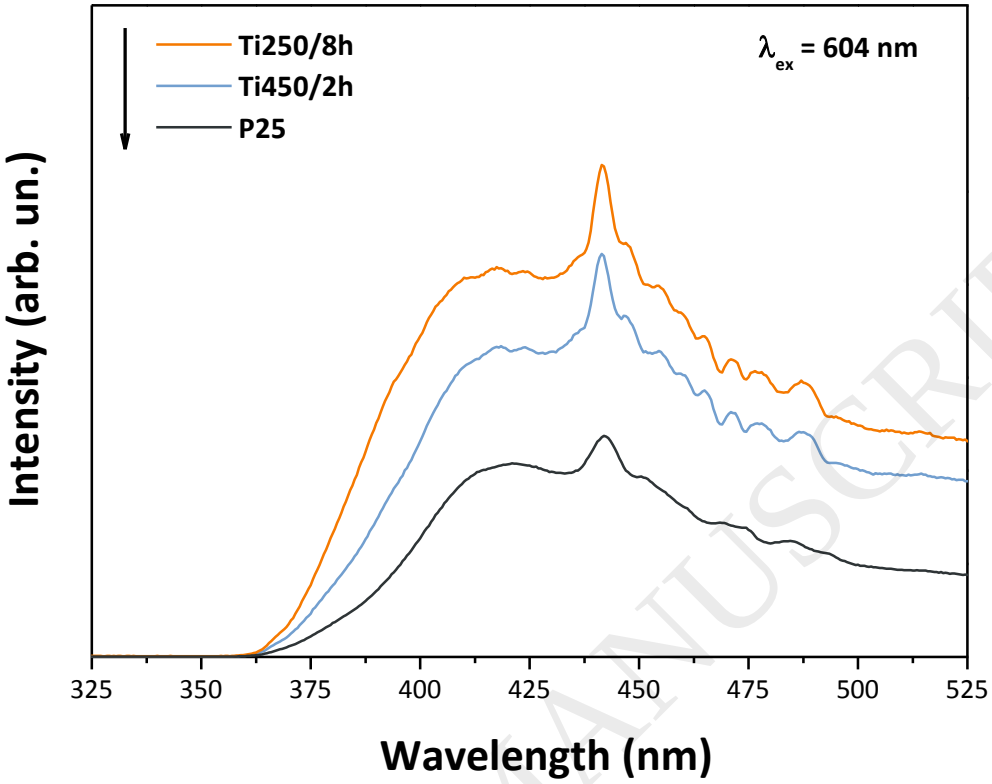

Scheme 1a

Band alignment of an anatase-rutile mixture in a RhB–TiO_2 system. The E_g of anatase (light blue) is from **HK-UV100**, that of rutile (dark blue) from **Ti250/8h**. Energy levels of TiO_2 are from Scanlon *et al*. [29], those of Rhb_0 and RhB* from Pan *et al* [109]. When irradiated by visible-light, RhB_0 is excited to RhB* (1). There is then an electron injection from the excited RhB* state into the CB of TiO_2 (2). (3) Recombination; (4) electron transfer from the CB of rutile to the CB of anatase and following transfer to the acceptor.

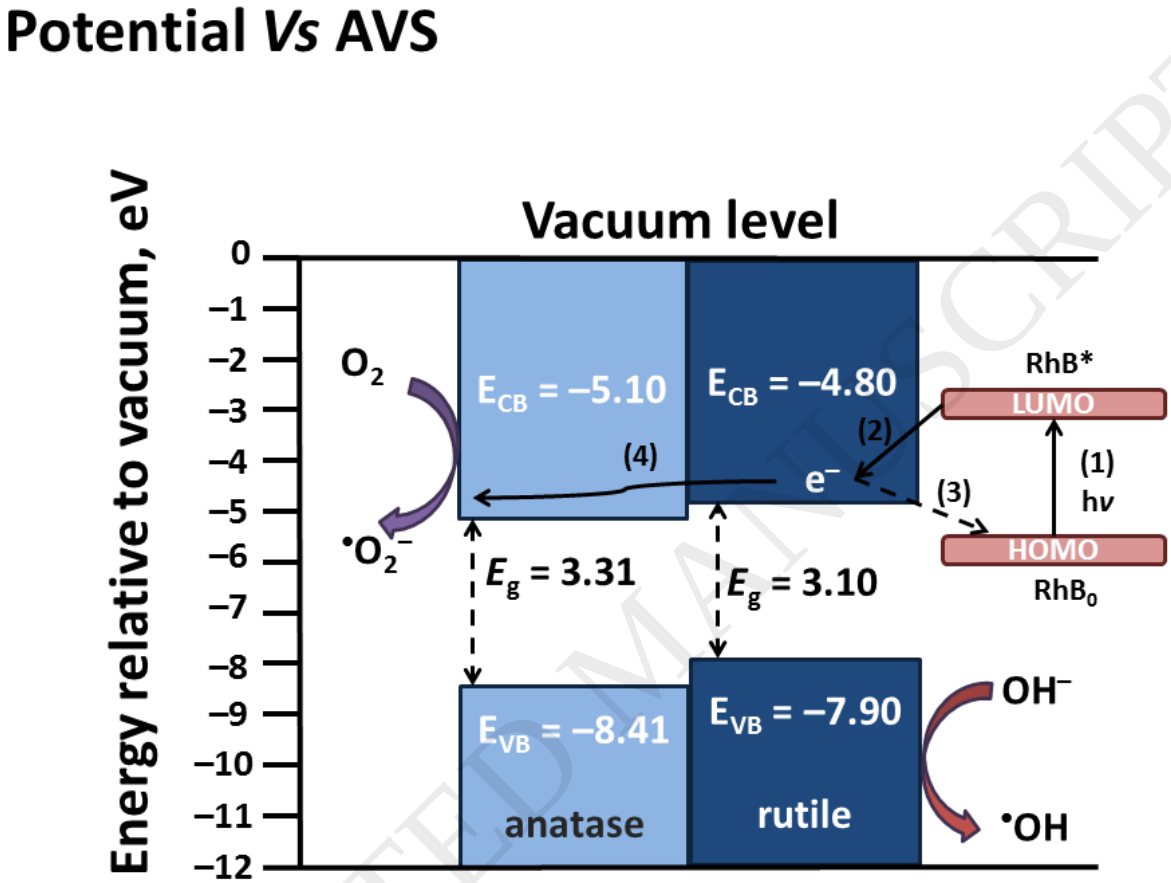

Note that, although the data reported here might not reflect a rigorous picture of the absolute values of CB and VB potentials, they provide a reasonable estimate of the relative band edge positions.

Scheme 1b

Band alignment of an anatase-rutile mixture, according to Scanlon *et al* [29]. The E_g of anatase (light blue) is from **HK-UV100**, that of rutile (dark blue) from **Ti250/8h**. (1) Visible-light excitation of TiO_2 and electron transferring from the VB to the CB of rutile, leaving a hole behind. (2) Electron transfer from the CB of rutile to the CB of anatase and following transfer to the acceptor.

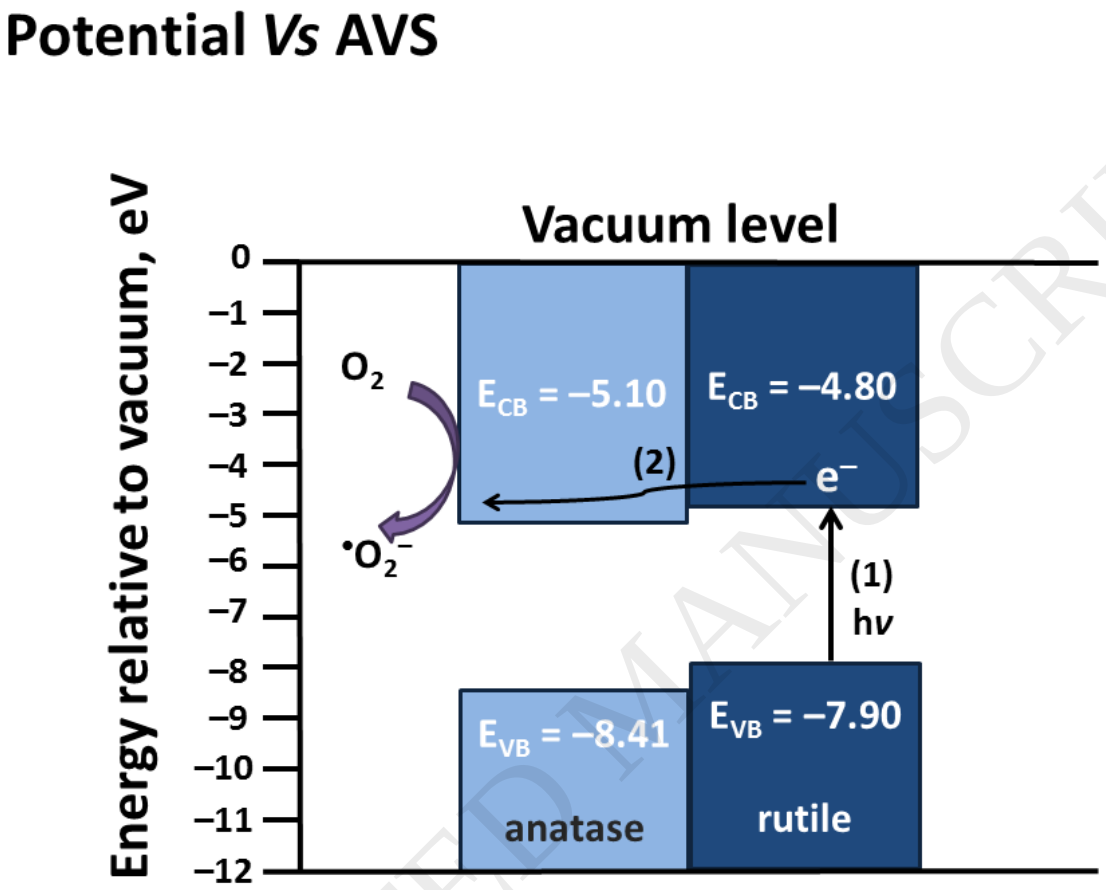

Note that, although the data reported here might not reflect a rigorous picture of the absolute values of CB and VB potentials, they provide a reasonable estimate of the relative band edge positions.